



A Numerical Analysis of Coal Burst Potential After the Release of the Fault-Slip Energy

Minghui Cao^{1,2} · Tongxu Wang² · Kesheng Li¹

Received: 19 July 2022 / Accepted: 5 January 2023 / Published online: 28 January 2023
© The Author(s), under exclusive licence to Springer-Verlag GmbH Austria, part of Springer Nature 2023

Abstract

Fault-slip instability due to mining is a critical factor leading to coal bursts. To better understand the impact of fault-slip release energy on a coal seam, a static and dynamic numerical calculation model was established using FLAC3D with geological conditions at a mine longwall face in contact with the fault. The change in coal seam parameters under a dynamic fault-slip load was studied, including the change in vibration velocity, displacement, abutment stress, and strain energy density. The coal seam impact hazard level was classified with the change in longwall–fault distance. Meanwhile, the numerical simulation results were compared and analyzed with microseismic monitoring records at the mining site to verify the accuracy of the results. The results showed that the increase in vibration velocity and displacement under the dynamic fault-slip load, and the sudden increase in abutment stress and strain energy density are precursors for coal bursts. As the longwall–fault distance decrease, the coal seam is in a high-stress state, and the internal strain energy accumulates. After the dynamic fault-slip load is transferred to the coal seam, the high static and strong dynamic loads are superimposed, leading to an increased risk of coal bursts. Additionally, the coal seam stability was analyzed under three influencing factors, including the seismic energy, the seismic source location, and the burial depth. This study contributes to a better understanding of the mechanism for dynamic fault-slip loading on coal seam disturbance and provides insight into the associated coal burst propensity assessment.

Highlights

- A dynamic calculation model for analyzing the stability of the coal seam under fault-slip load was established.
- The theory that destabilization of the coal seam with high static load and strong dynamic load was proposed and verified.
- With the decrease of longwall–fault distance, the coal seam is in the low coal burst risk, high coal burst risk, and post-damage stage.
- The stability of the coal seam was analyzed under three influencing factors, including the seismic energy, the seismic source location, and the burial depth.

Keywords Fault-slip · Dynamic analysis · Strain energy density · Coal bursts · Numerical analysis

✉ Minghui Cao
mhcao@cumt.edu.cn

¹ State Key Laboratory for Geomechanics and Deep Underground Engineering, China University of Mining and Technology, Xuzhou 221116, China

² College of Energy and Mining Engineering, Shandong University of Science and Technology, Qingdao 266590, China

1 Introduction

A coal burst is a sudden dynamic disaster that produces deformation and damage in a coal and rock mass while violently releasing energy. With the gradual expansion of coal mining into deeper and more geologically complex areas, coal bursts have become increasingly prominent, seriously limiting safe and efficient production in coal mines (Dai et al. 2021; Dou et al. 2014; He et al. 2018).

According to the characteristics of coal mine engineering, coal bursts could be classified into three types with respect to site-specific geological conditions. Type I: Coal bursts induced by material failure; Type II: Coal bursts induced by hard roof or floor; and Type III: Coal bursts induced by tectonic structures (Jiang et al. 2017a). Mining in the vicinity of a fault can induce coal burst disasters. The Rudna Mine in southwestern Poland was mined deeper than 1150 m, and a fault-slip due to mining activity resulted in the release of 2.84×10^9 J of energy, producing a local earthquake with a magnitude of 4.2 (Lizurek et al. 2015). Among the 50 coal burst accidents that occurred in the Longfeng coal mine, 72% occurred under the influence of faults, and 62% of the accidents occurred in the roadway near the fault (Kong et al. 2019). A coal burst due to a fault in the Qianqiu coal mine caused the death of 10 people and left 75 people trapped underground (Li et al. 2014). In a fault-slip coal burst, mining-induced fault-slip activation releases energy and causes damage to the coal and rock mass. Fault-slip coal bursts involve a significant energy release and serious destruction, and they are difficult to prevent (Li et al. 2019). The existence of fault structures significantly restrains the security of coal mining.

Microseismic monitoring and physical model tests can help effectively assess fault-slip coal burst accidents. This technology, including microseismic monitoring systems (Lu et al. 2019; Cheng et al. 2019) and seismic tomography (Wang et al. 2017a; Cai et al. 2014), can help investigate microseismic energy events around a fault in contact with a working face, and analyze the energy release process of fault activation. A similar simulation test has been used to study the overburden movement, abutment stress, and change in a fault displacement field and stress field when the longwall face in retreat mining encounters a fault (Jiang et al. 2017b; Wang et al. 2019). Wang et al. (2020) studied the evolution pattern of fault activation energy field based on stress and acoustic emission monitoring instruments. Energy accumulates before a fault-slip, and a large amount of energy is released at the moment of fault-slip.

The sudden change in a stress state caused by mining is the fundamental reason leading to fault-slip (Li et al. 2016, 2021). It is well accepted that a fault-slip will lead to a sudden drop in shear stress, release a large amount of energy, and trigger seismic waves (Brace et al. 1966; Ortlepp 2000; Sainoki et al. 2014a; 2015). Seismic source parameters, namely the seismic moment and moment magnitude, can be used to evaluate fault-slip risk (Xing et al. 2020). Sainoki et al. (2014b; c) investigated the effect of fault surface roughness on the magnitude of the seismic moment and fault activation release energy. Wei et al. (2020, 2021) analyzed the magnitude of the energy released during fault activation when the longwall face advanced in the fault direction and also studied the effect of the change of fault parameters on

the energy release of the fault. However, numerical analyses under static conditions are unable to investigate the impacts of fault-slip vibration waves on the stability of underground mining. As a result, research on the effects of fault activation and dynamic loading on coal and rock mass disturbances has been carried out. Wang and Cai (2017b) investigated the effect of seismic waves on the excavation of a cavern. Sainoki et al. (2018) analyzed the damage around an underground cavern caused by seismic waves due to fault-slip and proposed a plastic strain energy damage assessment method. Gao et al. (2021) analyzed the characteristics of fault-slip seismic waves and the effect of seismic waves on rockbursts triggered by dynamic processes. Jiang et al. (2020) calculated the magnitude of a fault activation seismic moment by static and dynamic numerical simulation and analyzed the influence of seismic waves on the disturbance of coal and rock mass in mining longwall face to determine the coal burst potential.

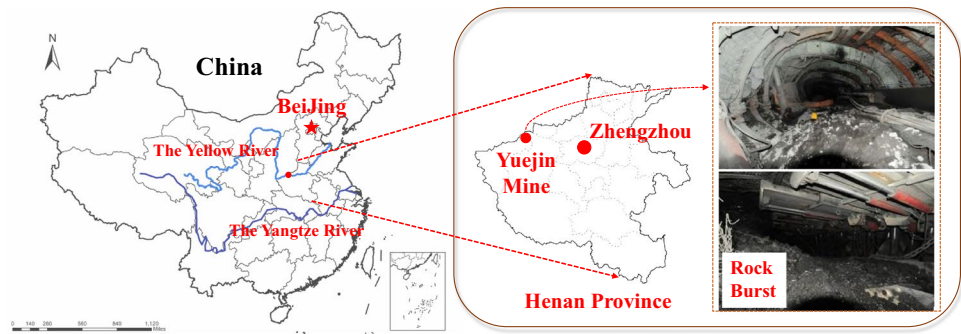
In summary, the fault-slip mechanism and fault activation release energy under mining induction have been widely investigated. Nevertheless, the perturbation effect of dynamic fault-slip load on coal seam have not been widely discussed. This study, numerical methods are used to focus on the impact of fault-slip vibration on longwall mining disturbance. A 3D model is built with FLAC3D to analyze the coal burst potential induced by the activation and release of the energy in a fault during a retreat-mining operation. The numerical model evaluates the coal seam stability under the influence of fault-slip seismic energy, including the vibration velocity, vibration displacement, abutment stress, and strain energy density (SED). Next, the results are compared with field microseismic monitoring to verify the reliability of the numerical simulation. Meanwhile, the stability of the coal seam is analyzed under different conditions of seismic source energy, seismic source location, and mining depth. This investigation provides some theoretical explanation of the mechanism of coal bursts induced by fault reactivation.

2 Engineering Background

2.1 Longwall Face Introduction

The Yuejin coal mine is located in the Yima coalfield, Yima City, Henan Province, China, as shown in Fig. 1. The F16 large reverse-thrust fault is located at the southern boundary of the Yima coalfield, which leads to complex geological conditions in the coalfield. The F16 reverse-thrust fault is formed under huge compaction and the over thrusting effect of the thrust-nappe tectonic system (Lu et al. 2019). Small associated faults are extremely developed in the coalfield due to the influence of F16 faults.

Fig. 1 Overview of Yima coal mine field location



The mining depth of the 25,110 longwall face in the Yuejin coal mine is approximately 800–1200 m. The thickness of #2–1 coal seam is 7.4–13.8 m with an inclination angle of 12°. The immediate roof is mudstone of 18 m thickness, the primary roof is sandstone of 190 m thickness, the immediate floor is mudstone of 4 m thickness, and the primary floor is sandstone of 26 m thickness. To the north of the 25,110 longwall face is the 25,090 longwall face, and the south approaches the F16 fault. F16 reverse-thrust fault trending in the EW direction, with a fault dip of 30°–75°. The dip angle of the F16 fault near the 25,110 face is 50°–65°.

2.2 Microseismic Monitoring

Using a microseismic monitoring system, the microseismic events generated during excavation and initial mining were evaluated at the 25,110 longwall face of the Yuejin coal mine affected by the F16 reverse-thrust fault, as shown in Fig. 2. Figure 2a shows that low-energy seismic source events ($E < 10^3$ J) were generated during the initial excavation stage of the roadway due to far away from the F16 fault. As the distance between the excavation position and the fault became less than 100 m, the seismic source

density gradually increased, and a large number of microseismic events exceeding 10^5 J were generated, even reaching 10^6 – 10^7 J. In addition, almost all high-energy sources ($E > 10^5$ J) were clustered around the F16 fault zone closest to the 25,110 longwall face. Therefore, continuing excavation produces disturbing effects, activating fault instability and thus inducing a large number of high-energy microseismic events.

Figure 2b shows the microseismic monitoring records during the retreat-mining operation of the longwall face. The distance between the mining longwall face and the F16 fault gradually increased. At the beginning of mining, the longwall–fault distance was less than 100 m. The disturbance generated by mining, as well as the change in the original rock stress and the collapse of the overlying rock layer after mining, led to the activation and destabilization of the F16 fault. A fault-slip releases a large amount of energy and generates a significant number of high-energy microseismic events. Therefore, microseismic events near the fault with energy levels of 10^7 J or even greater than 10^8 J were generated at the onset of mining. As the longwall–fault distance increases, the density of microseismic events decreases, and the energy level of the source also reduces to 10^5 J.

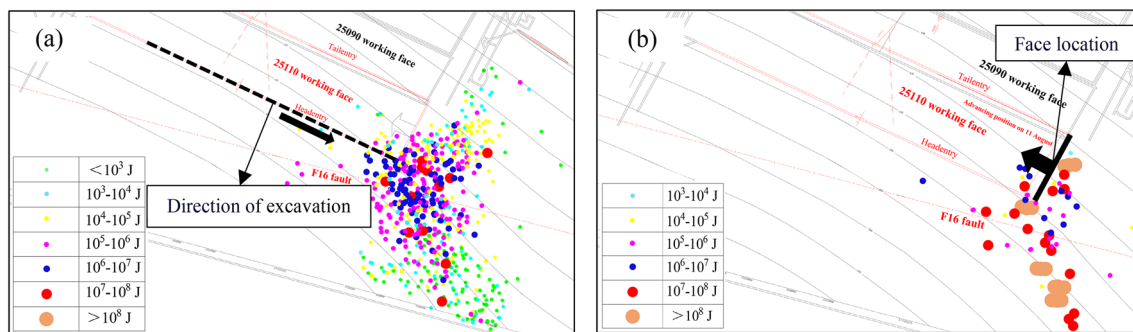
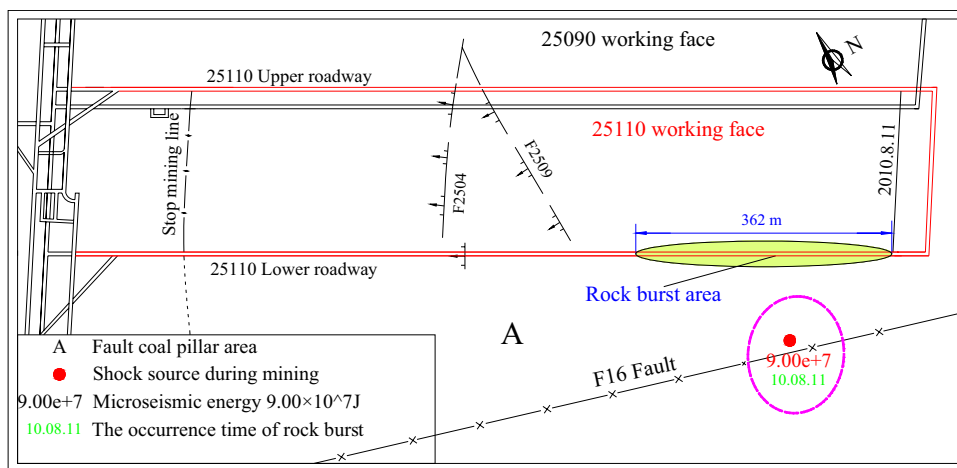


Fig. 2 Planar distribution of microseismic sources during excavation and initial mining at the 25,110 longwall face. **a** Excavation periods. **b** Initial mining periods (According to Lu et al. 2019)

Fig. 3 “8.11” impact accident location



2.3 '8.11' Impact Accident

On August 11, 2010, the "8.11" severe coal burst accident occurred at the early stage of mining of the 25,110 longwall face, with a seismicity magnitude of 2.7 and released energy of 9×10^7 J. Figure 3 shows the location of the "8.11" impact accident. The coal burst accident occurred at 32 m along the lower roadway, resulting in damage to the 362 m long roadway. At the time of this accident, the distance between the longwall face and the fault was less than 100 m. Fault-slip was an essential factor leading to this accident.

3 Simulation Methodology

3.1 Static Analysis Model

Although the coal burst site location shown in Fig. 3 is located at the entry ribs, the impact essentially is a change in the stability of the coal seam below the fault during the mining influence. Therefore, in this study, a simplified version of

the numerical calculation model is established using FLAC to simulate and analyze the stability of the coal seam as the longwall–fault distance decreases. The FLAC3D numerical model is established according to the geological conditions of the 25,110 longwall face, and static and dynamic analyses are carried out. Figure 4 shows the model with dimensions of 450 m (length) \times 400 m (width) \times 140 m (height). The depth of the simulated coal seam is 800 m. A vertical stress of 16 MPa is applied at the top boundary of the model by assuming a rock density of 2500 kg/m³ above the coal seam. The side pressure coefficient is 1.2. The fault surface is established using the interface command, with a fault dip of 50° and a drop of 10 m. The Mohr–Coulomb strength criterion is used in the model, the coal and rock parameters are shown in Table 1, and the Coulomb shear model is adopted for the fault surface. The main mechanical parameters of the fault (Jiao et al. 2021; Li et al. 2021) are as follows: normal stiffness is 5 GPa, shear stiffness is 2 GPa, friction angle is 15°, and cohesion is 0.3 MPa.

In the static analysis model, the bottom boundary of the model is fixed, the top boundary is free, and the surrounding

Fig. 4 Numerical model

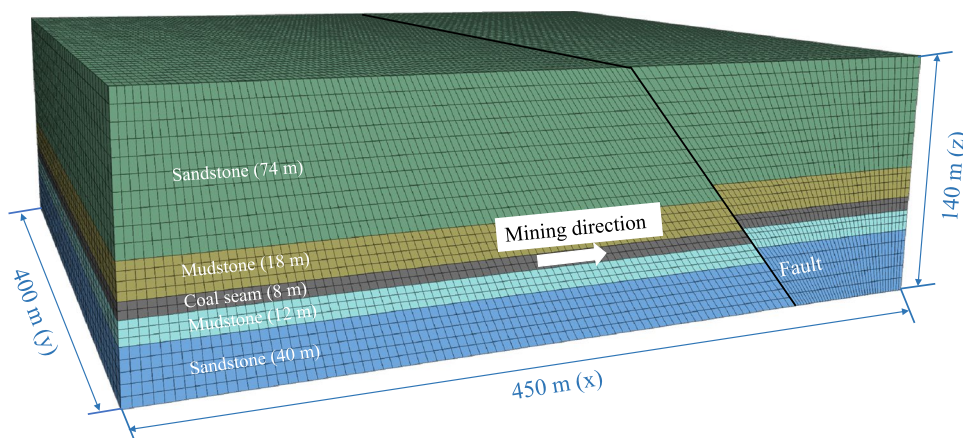
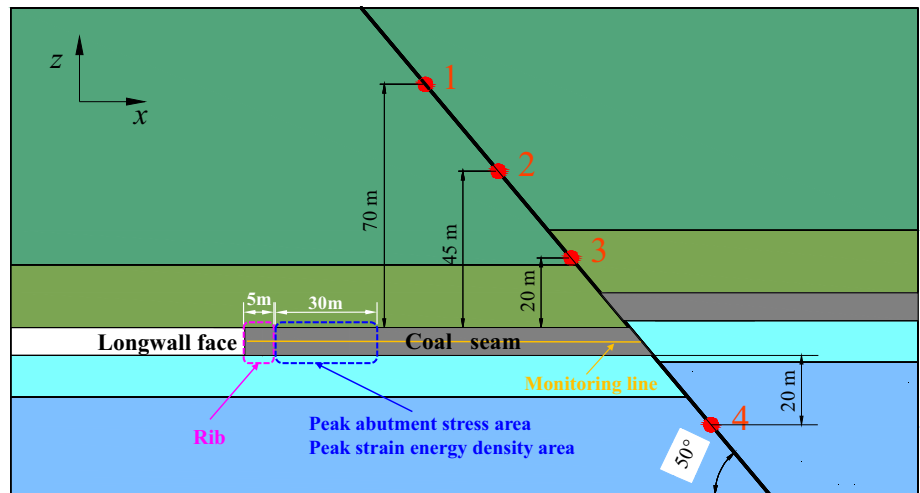


Table 1 Rock mass properties

Lithology	Density (kg/m ³)	<i>K</i> (GPa)	<i>G</i> (GPa)	<i>c</i> (MPa)	φ (°)	σ_t (MPa)
Sandstone1	2650	14.2	9.7	6.5	35	4.2
Mudstone1	2530	6.2	3.9	3.0	32	1.5
Coal	1450	1.8	1.2	1.4	28	1.2
Mudstone2	2550	6.7	4.2	3.2	33	1.7
Sandstone2	2650	14.2	9.7	6.5	35	4.2

Fig. 5 Diagram of monitoring points and monitoring line arrangement. The monitoring points are located at 70 m, 45 m, and 20 m from the roof of the coal seam, and 20 m from the floor of the coal seam, as shown in points 1, 2, 3, and 4. The rib and the peak abutment stress area at 35 m ahead of longwall face is the key area of coal seam studied in this study



boundary is fixed in the horizontal direction and free in the vertical direction. The longwall face is advanced from the left of the model in the *x*-axis direction, and the mining width is 140 m with a depth of 20 m. Due to the boundary effect, the mining area is not less than 50 m from the model boundary. As shown in Fig. 5, a monitoring line is arranged inside the coal seam in front of the longwall face to monitor the changing internal parameters, such as vibration velocity, vibration displacement, abutment stress, and SED. Four monitoring points are arranged on the fault face, and the monitoring points are located at 70 m, 45 m, and 20 m from the roof of the coal seam, and 20 m from the floor of the coal seam, as indicated by points 1, 2, 3, and 4, respectively.

The user-defined FISH program implements the calculation of SED. The equation for calculating the SED in the FLAC3D model is as follows

$$W = [\sigma_1^2 + \sigma_2^2 + \sigma_3^2 - 2\nu(\sigma_1\sigma_2 + \sigma_2\sigma_3 + \sigma_3\sigma_1)]/2E_0, \quad (1)$$

where $\sigma_1, \sigma_2, \sigma_3$ are the maximum, intermediate and minimum principal stresses; ν and E_0 are the Poisson's ratio and the elastic modulus, respectively.

Static analysis process: (1) Establish the initial model, and set up monitoring points and monitoring lines. (2) Initial stress field balance, speed and displacement reset. (3) Progressive excavation of the longwall face, and static calculation balance. (4) Output monitoring data.

3.2 Validation Analysis of Static Analysis Model

The Coulomb shear model is adopted for the fault surface. According to the Coulomb shear strength criterion, the shear force $F_{s \max}$ required for the relative sliding of the contact surface can be obtained as (Itasca 2009):

$$F_{s \max} = cA + F_n \tan \phi, \quad (2)$$

where $F_{s \max}$ is the maximum shear strength; c is the cohesive strength; ϕ is the interface friction angle; F_n is the normal force calculated from the numerical step.

When the shear force on the contact surface is greater than or equal to the maximum shear force ($F_s \geq F_{s \max}$), the state of the interface nodes changes to the Coulomb slip state.

Figure 6 shows the process of fault-slip when the longwall–fault distance decreases. The fault-slip when the longwall–fault distance is less than 120 m. When the longwall–fault distance is 100 m, 80 m and 60 m, the fault at the location of monitoring points 1, 2 and 3, respectively, undergoes fault-slip, as shown in Fig. 6c, d, e. The fault at the floor plate slips when the longwall–fault distance is 0 m, as shown in Fig. 6h. The shear-slip area of the entire fault gradually increases as the longwall–fault distance decreases.

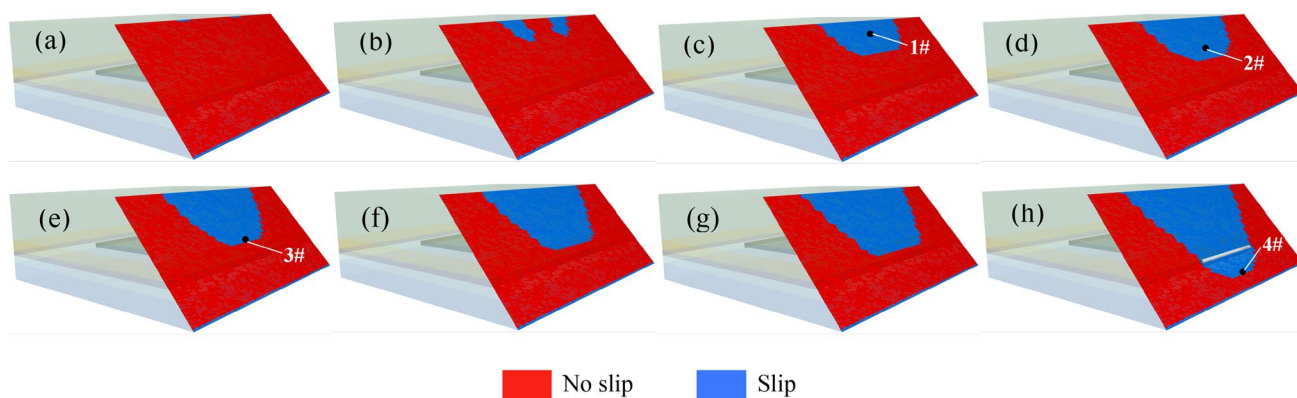


Fig. 6 The process of fault-slip when the longwall–fault distance decreases. **a–h** The fault distance at the longwall face is 140, 120, 100, 80, 60, 40, 20, 0 m

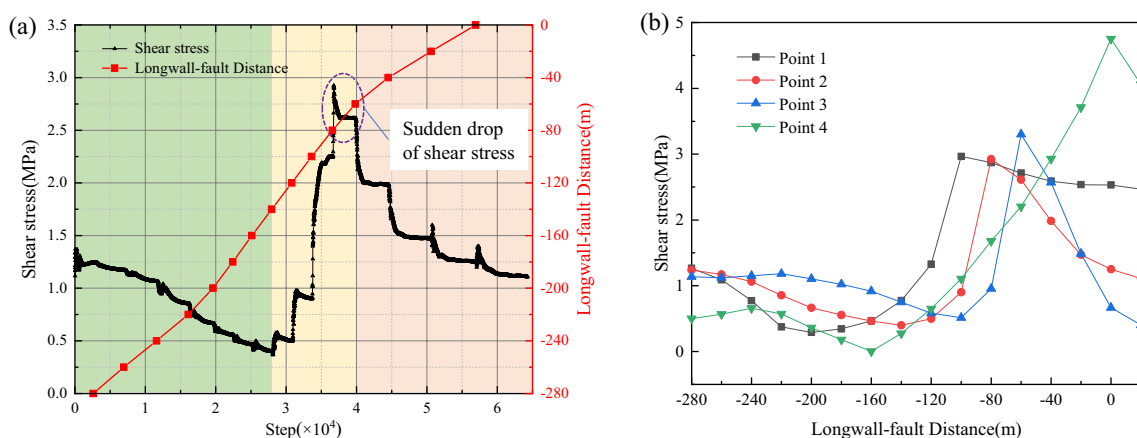


Fig. 7 Shear stress change law with the longwall–fault distance decrease. **a** Shear stress change law of monitoring point 2. **b** Shear stress change law of monitoring points 1, 2, 3 and 4

At the time of the "8.11" severe coal burst accident, the distance between the longwall face and the fault was less than 100 m. Therefore, the numerical simulation results are in good agreement with the field monitoring results.

The shear stress evolution process of the fault can effectively reflect the fault stability (Wei et al 2020; Wang et al 2021a, b). Figure 7a shows the evolution of the shear stress at monitoring point 2 as the longwall–fault distance decreases. The shear stress at point 2 diminishes gradually as the longwall–fault distance decreases to 140 m. When the longwall–fault distance is 140–80 m, the shear stress increases rapidly at first, and then gradually reaches the peak (2.92 MPa) at 80 m and drops suddenly. The shear stress decreases continuously as the longwall–fault distance decreases below 80 m.

Figure 7b shows that the shear stress trend at points 1, 3 and 4 is similar to that of point 2 as the longwall–fault distance decreases. When the longwall–fault distance is 100, 80, 60 and 0 m respectively, the shear stresses at points 1, 2,

3 and 4 reach the peak strength and drop abruptly, leading to fault-slip destabilization.

Comparing Figs. 6 and 7, it can be seen that the shear stress trend is consistent with the slip process of the interface contact surface in the fault.

The sudden increase in shear stress is a precursor to fault-slip instability (Wang et al 2021b). As the longwall–fault distance decreases, the maximum shear strength of the fault gradually decreases due to the influence of mining. Fault-slip occurs as the shear stress exceeds the maximum shear strength ($F_s \geq F_{s \max}$). The fault-slip will lead to a sudden drop in shear stress, release a large amount of energy, and trigger seismic waves (Brace et al. 1966; Ortlepp 2000; Sainoki et al. 2014a; 2015).

3.3 Dynamic Analysis Model

Dynamic research is employed to analyze the stability of the coal seam under the influence of fault activation energy.

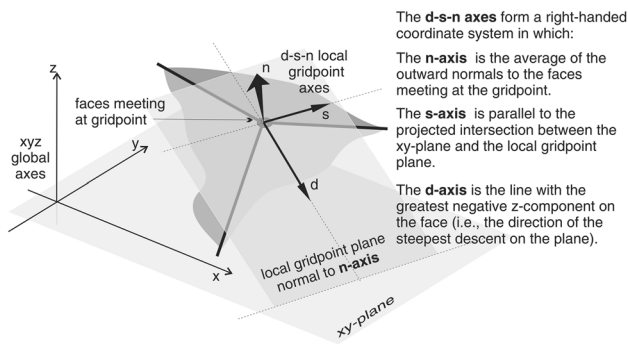


Fig. 8 Interface contact direction (Itasca 2009)

Figure 8 shows the direction of the interface contact surface in FLAC3D, where *n* is the normal direction, *d* is the dip direction, and *s* is the strike direction. When shear-slip instability occurs in a fault, a pair of shear stresses parallel to the fault surface and another pair of stresses perpendicular to the fault surface are released (Gao et al. 2021). In other words, the released fault-slip energy is not only in the dip direction of the fault plane but also in the normal direction of fault plane. Therefore, when the dynamic fault-slip load is applied to the interface contact surface, vibration waves along the normal and inclined directions of the contact surface simulate the process of fault activation release energy.

The vibration waveform is different under various rupture modes such as coal seam rupture, roof fracture, and fault-slip. The impact vibration wave generated by a fault-slip has a more prolonged action time and a higher peak intensity. In general, the source peak vibration velocity for fault-slip shock waves is in the range of 10⁰ m/s.

As shown in Fig. 2, a large amount of energy is released around the F16 fault, while mining the 25,110 longwall face. Most of the microseismic energy is less than 10⁶ J, but there are also high-energy microseismic events with energy greater than 10⁷ J. Therefore, a seismic source energy of 10⁷ J is selected analyze the effect of the dynamic load of fault activation on the coal seam disturbance and simultaneously verify the reasonableness of model parameter selection.

The seismic source is generated by fault activation slip, so the velocity waveform can be used to establish the source function (Liu et al. 2019). The source time function of the velocity wave is set according to Eq. (3).

$$A(t) = \begin{cases} \frac{1}{2}A_0[1 - \cos(2\pi ft)] & 0 \leq t \leq 0.1 \\ 0 & t > 0.1, \end{cases} \quad (3)$$

where *A*₀ represents the source peak vibration velocity, according to the fault activation release energy size, refer to Table 2 to set the value; *f* is the vibration wave frequency,

Table 2 Shock wave parameter selection

No	Energy (J)	Density (kg/m ³)	Wave velocity (m/s)	<i>A</i> ₀ (m/s)
1	10 ⁴	2500	4300	0.93
2	10 ⁵	2500	4300	2.71
3	10 ⁶	2500	4300	5.58
4	10 ⁷	2500	4300	9.30
5	10 ⁸	2500	4300	15.10

taking the value of 10 Hz, dynamic load action time is one cycle 0.1 s.

According to the results in Sect. 3.2, the fault at the location of monitoring points 1, 2 and 3 undergoes fault-slip when the longwall–fault distance is 100 m, 80 m and 60 m, respectively. Therefore, the dynamic load position is applied to the fault at 45 m above the coal seam, as indicated by point 2 in Fig. 5.

To reduce the reflection of seismic waves during the model calculation and to improve the calculation accuracy, it is necessary to choose reasonable boundary conditions in FLAC3D for dynamic analysis (Jiang et al. 2020). The quiet boundary is used to reduce wave reflections at the boundary. The quiet boundary of the model is equipped with an independent damping device (mechanical viscosity damping device) in the normal and shear directions that can effectively absorb the energy of the seismic wave when the incident angle is greater than 30° (Itasca 2009). Considering the self-oscillation effect of the material, Rayleigh damping is chosen for the dynamic analysis. For geotechnical materials, the critical damping ratio is generally 2–5%. The Mohr–Coulomb elastic–plastic constitutive model is used in the dynamic analysis, and the energy is dissipated in the plastic flow phase, so the critical damping ratio is set to 5%, and the minimum center frequency is set to 250 Hz.

Dynamic analysis process: (1) Call static calculation results. (2) Set dynamic on, and apply dynamic load. (3) Balance of dynamic calculation. (4) Output monitoring data.

4 Stability Analysis of Coal Seam Under Fault-Slip Load

This section discusses the results of fault-slip load disturbance on coal seam, mainly focusing on the vibration velocity, displacement, abutment stress, and SED indicators.

4.1 Vibration Velocity

Under the influence of mining, fault-slip release energy, and the energy is transferred outward in the form of a shock

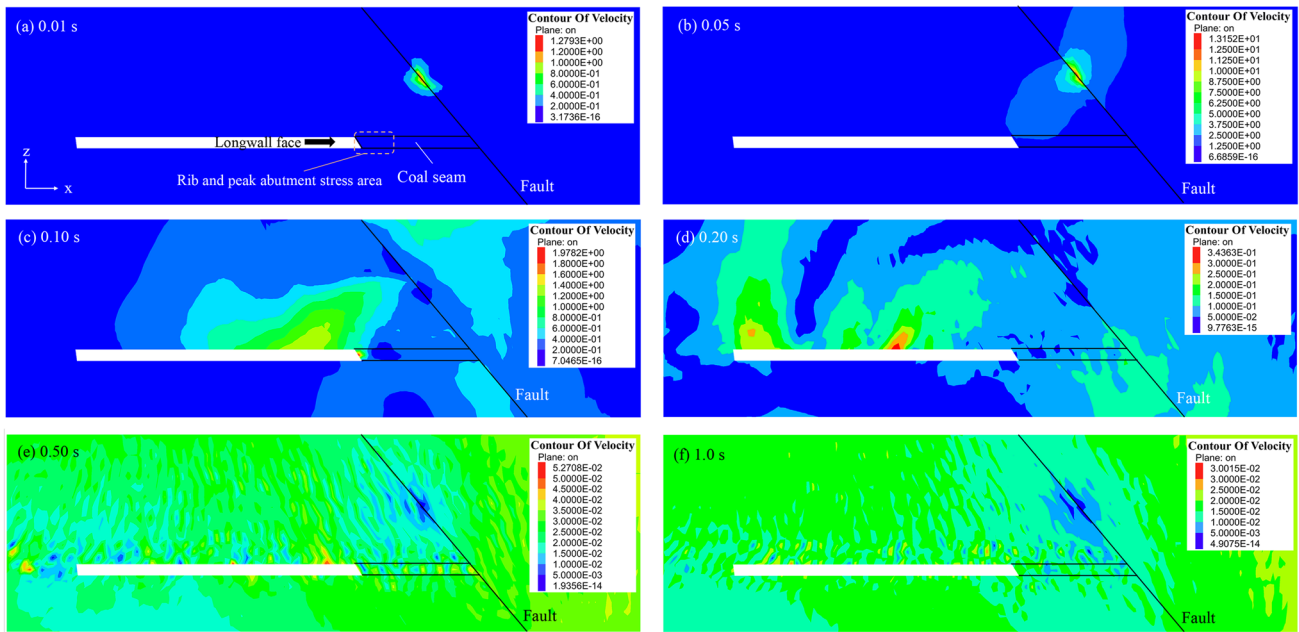


Fig. 9 Cloud diagram of velocity propagation at the longwall–fault distance is 80 m. **a** Time is 0.01 s. **b** Time is 0.05 s. **c** Time is 0.10 s. **d** Time is 0.20 s. **e** Time is 0.50 s. **f** Time is 1.0 s

wave. When the shock wave reaches the coal seam in front of the longwall face, the vibration speed of the coal seam increases, resulting in a decrease in the stability of the coal and rock mass.

Figure 9 shows the fault-slip velocity propagation graph when the longwall–fault distance is 80 m. After the dynamic load is applied, the vibration velocity wave propagates to the rock layers above and below the fault and dissipates rapidly. At a propagation time of 0.05 s, the vibration wave begins to have a disturbing influence on the coal seam in front of the longwall face. As the propagation time increases to 0.10 s,

the vibration velocity of the coal seam increases, and the dynamic fault-slip load has a more significant disturbance effect on the coal seam. When the propagation time exceeds 0.20 s, the influence of the dynamic fault-slip load on the coal seam is gradually weakened.

Figure 10 shows the vibration velocity curve in the peak abutment stress zone at different phases of mining. The peak abutment stress area is introduced in the later analysis (Sect. 4.3). After the action of the dynamic load for 0–0.2 s, the vibration velocity in the peak abutment stress zone appears to have large fluctuations. When the longwall–fault

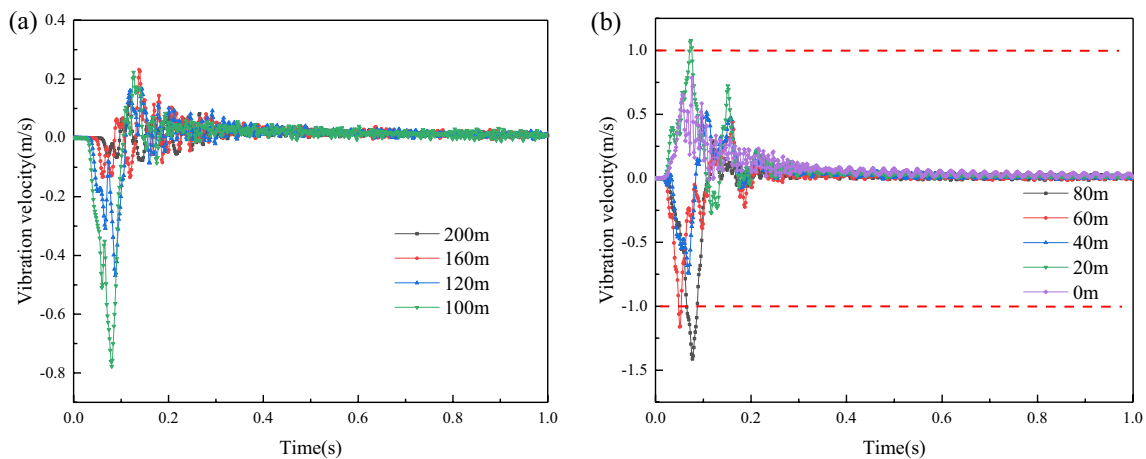


Fig. 10 Vibration velocity variation curve with the longwall–fault distance decrease. **a** Longwall–fault distance is 200–100 m. **b** Longwall–fault distance is 80–0 m

distance is 200 m, 140 m, and 100 m, the distance between the hypocenter of the earthquake and the rib of the longwall face is 169.73 m, 113.46 m, and 79.05 m, respectively, and the peak particle velocity (PPV) of the peak abutment stress zone is 0.14 m/s, 0.22 m/s, and 0.78 m/s, respectively. Therefore, with the decrease in the longwall–fault distance, the PPV increases. When the longwall–fault distance is 80 m, the hypocenter is closer to the longwall face at a distance of 64.31 m, and the PPV reaches 1.41 m/s. With the longwall–fault distance continuing to decrease from 80 to 0 m, the PPV does not significantly increase and remains stable at approximately 1.0 m/s.

Brinkmann (1987) stated that a PPV of approximately 1.0 m/s is sufficient to induce a coal burst, resulting in severe roadway or rock fall deformation. In particular, the frequency of coal bursts is associated with high PPV values in overstressed coal seam zones (Mutke et al. 2015). The PPV is less than 0.78 m/s when the longwall–fault distance exceeds 100 m, resulting in a lower risk of coal burst. When the longwall–fault distance is less than 80 m, the fault-slip position is closer to the longwall face, and the PPV reaches 1.41 m/s, as shown in Fig. 10b. Hence, it can be assumed that when the seismic source is far from the longwall face, the vibration waves dissipated in the transmission, and there is no significant effect on the coal seam. However, when the longwall–fault distance is less than 80 m, the seismic wave has a significant perturbation effect on the coal seam. Seismic hazard criteria based on the analysis of one seismic parameter can lead to incorrect or low-quality estimations of seismic and coal burst hazards (Mutke et al. 2015). For this reason, further analyses of coal burst hazards using abutment stress, SED and other indicators will be carried out later.

4.2 Displacement in the Rib of Longwall Face

Plastic damage occurs to the rib in front of the longwall face after mining. Rib damage produces displacement toward the free surface direction, resulting in displacements that are skewed toward the panel. The vibration velocity of the coal seam increases due to the influence of the dynamic load due to fault activation, which intensifies the damage to the rib. Therefore, by analyzing the magnitude of horizontal displacement in the rib of the longwall face, the damage of the coal and rock mass can be derived, and the danger can be judged.

Figure 11 presents the horizontal displacement curve of the rib with the longwall–fault distance. When the longwall–fault distance is greater than 80 m, the barrier effect of the fault on mining is not clear, and there is only minor damage to the rib. When the longwall–fault distance is 60 m, the rib is under a greater load from the combined effect of relative fault-slip and extra-thick rock strata, and is in the ultimate stable state. After the dynamic fault-slip load, the plastic destruction area of the rib increases, which leads to a larger displacement of the rib. When the longwall–fault distance is less than 40 m, the rib shows clear plastic failure and large displacement under the influence of mining. The dynamic load has a weak effect on the rib disturbance that has already caused plastic damage. Therefore, the increment of horizontal displacement for a rib under dynamic load is small.

From the content in Sect. 4.1, it can be seen that the vibration velocity fluctuates significantly within 0–0.2 s after the seismic wave is applied. At the same time, the rib is affected by the dynamic fault-slip load when the seismic

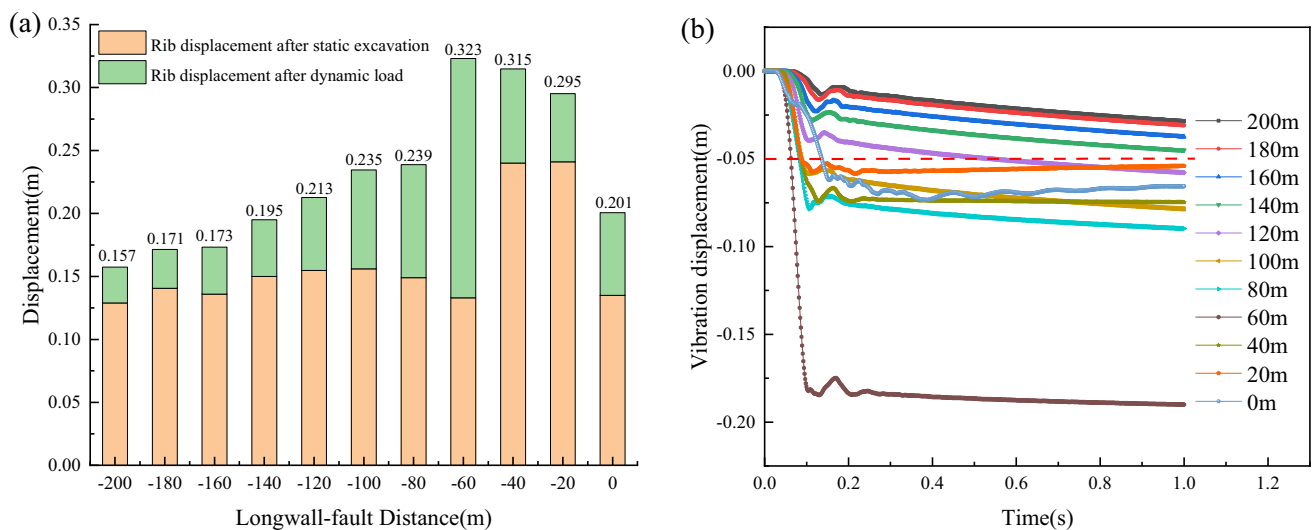


Fig. 11 Horizontal displacement variation curve of rib with the longwall–fault distance decrease. **a** Horizontal displacement of rib during static excavation and dynamic loading. **b** The evolution process of horizontal vibration displacement of rib under dynamic load

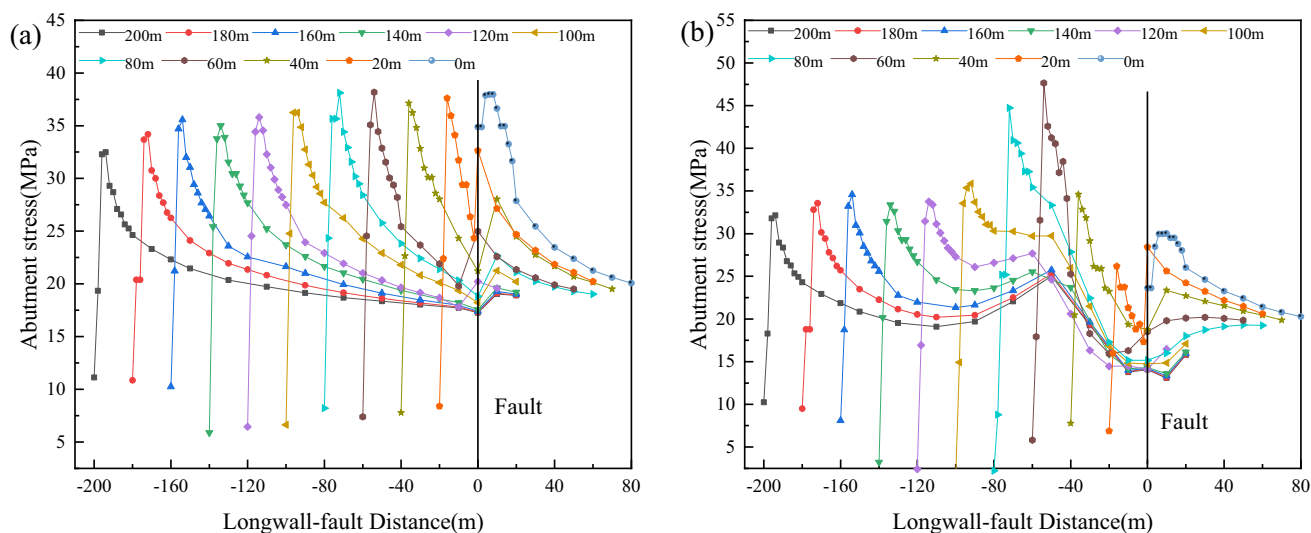


Fig. 12 Evolution of coal seam abutment stress before and after dynamic load. **a** Before dynamic load. **b** After dynamic load

wave acts for 0–0.2 s, and a large displacement occurs along the horizontal direction, as shown in Fig. 11b. The dynamic fault-slip load can have a large impact on the coal seam in a short period of time.

4.3 Abutment Stress

Figure 12 shows the evolution of abutment stress in the coal seam at different phases of mining under static and dynamic loadings. The abutment pressure peak area is located 5–10 m in front of the longwall face. Before the dynamic fault-slip load, the peak abutment stress (PAS) of the coal seam is 34.2 MPa, 35.0 MPa, and 38.1 MPa when the longwall–fault distance is 200 m, 140 m, and 80 m, respectively, as shown in Fig. 12a. It can be seen that with the decrease in the longwall–fault distance, the PAS gradually increases. When the longwall–fault distance is 60 m and 20 m, the PAS is 38.2 MPa and 37.6 MPa. When the longwall–fault distance is less than 80 m, the change in PAS is insignificant and remains approximately 37–38 MPa. The increased load from the combined effect of the fault-slip and extra-thick rock strata movement causes the abutment stress of the coal seam to increase. Therefore, when the longwall–fault distance is less than 80 m, the coal seam appears to concentrate the stress, leading to a risk of coal burst.

The abutment stress of the coal seam is affected by the dynamic fault-slip load, as shown in Fig. 12b. When the longwall–fault distance is greater than 100 m, the PAS of the coal seam shows a subtle change due to the effect of energy attenuation. The PAS is 44.7 MPa and 47.6 MPa, respectively, when the longwall–fault distance is 80 m and 60 m, with the dynamic fault-slip load disturbance; the PAS

increases by 6.6 MPa and 9.4 MPa, respectively, compared to the situation without a dynamic load. The sharp increase in PAS of the coal seam leads to significant coal burst potential. When the longwall–fault distance is 40, 20, and 0 m, the PAS decreases by 2.5 MPa, 11.4 MPa, and 8.0 MPa, respectively, after the dynamic load, which are decreases of 6.7%, 30.3%, and 21%, respectively. The abutment stress of the coal seam drops suddenly, which indicates that the coal seam has plastic damage.

4.4 SED

The SED index is an essential indicator for analyzing the safety of coal and rock mass (Wang et al. 2015; Miao et al. 2016; Xiao et al. 2021). When affected by mining activities, fault-slip events release large amounts of energy and trigger seismic waves (Sainoki et al. 2014a; Jiang et al. 2020). Consequently, the law of SED change in a coal seam after a dynamic fault-slip load is investigated.

Figure 13 shows the distribution pattern of the SED stored inside the coal seam before and after the dynamic fault-slip load at different phases of mining. After the action of the dynamic load, the SED remains stable at a longwall–fault distance of 100 m, concentrates and accumulates at a distance of 80 m, and releases suddenly at a distance of 20 m. To analyze the magnitude of the change in SED values before and after the action of dynamic load, monitoring lines are arranged inside the coal seam, as shown in Fig. 13a-1.

Figure 14 shows the magnitude change of SED in the coal seam before and after the dynamic load. When the longwall–fault distance is 200 m, the peak strain energy density (PSED) inside the coal seam is 177.49 kJ/m³ and 172.91 kJ/

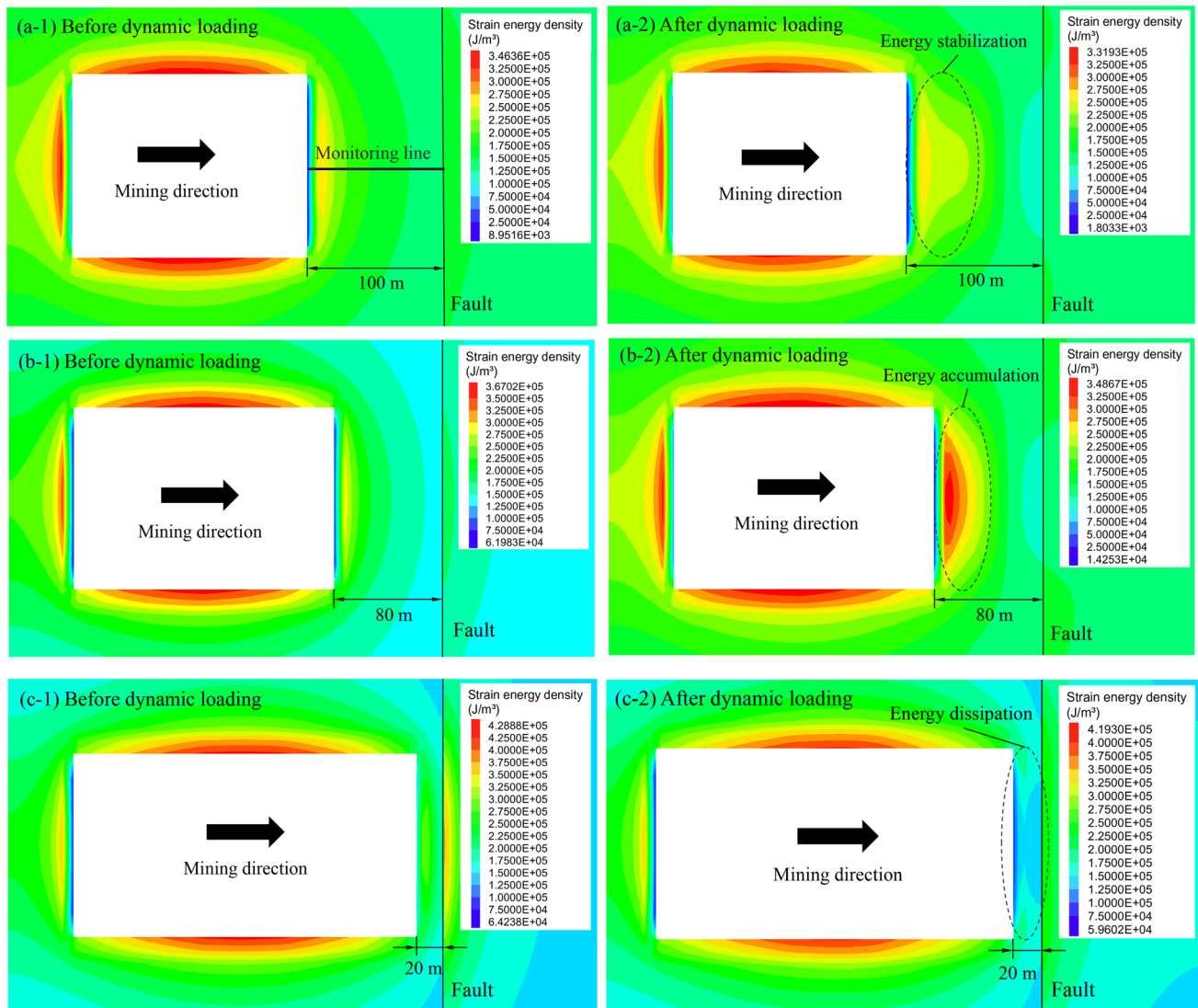


Fig. 13 The SED cloud diagram of coal seam before and after dynamic load. **a** Longwall–fault distance is 100 m. **b** Longwall–fault distance is 80 m. **c** Longwall–fault distance is 20 m

m^3 before and after the action of the dynamic load, as shown in Fig. 14a. The position of the PSED remains relatively stable. Therefore, the effect of dynamic load on coal seam disturbance is insignificant. The coal seam exhibits strain energy accumulation when the longwall–fault distance is 100 m, which is affected by the relative slip and barrier effect of the fault. The PSED stored inside the coal seam before the impact of dynamic load disturbance is 238.82 kJ/m^3 ; after the dynamic load, the PSED decreases to 230.72 kJ/m^3 . Strain energy accumulation occurs inside the coal seam 20–60 m in front of the longwall face. It can be seen that the coal seam accumulates energy and remains stable.

The PSED increases from 249.10 kJ/m^3 to 328.04 kJ/m^3 after the dynamic load when the longwall–fault distance is

80 m, as shown in Fig. 14c. The PSED increases sharply, and its position extends to the inside of the rib. Strain energy accumulation occurs inside the coal seam 8–40 m in front of the longwall face. When the longwall–fault distances are 40 m, 20 m, and 0 m, the PSED is 243.62 kJ/m^3 , 241.15 kJ/m^3 , and 242.88 kJ/m^3 before the dynamic load, respectively; after the dynamic load, the sudden drop in PSED is 45.61 kJ/m^3 , 113.92 kJ/m^3 , and 77.23 kJ/m^3 , respectively.

As the longwall–fault distance decreases, the trend of the PAS of the coal seam is similar to that of the PSED, i.e., slow decline–sharp increase–quick release, as shown in Fig. 15. The rapid energy accumulation inside the coal seam is the precursor to coal bursts. Therefore, the coal burst risk is classified according to the energy changes in the coal

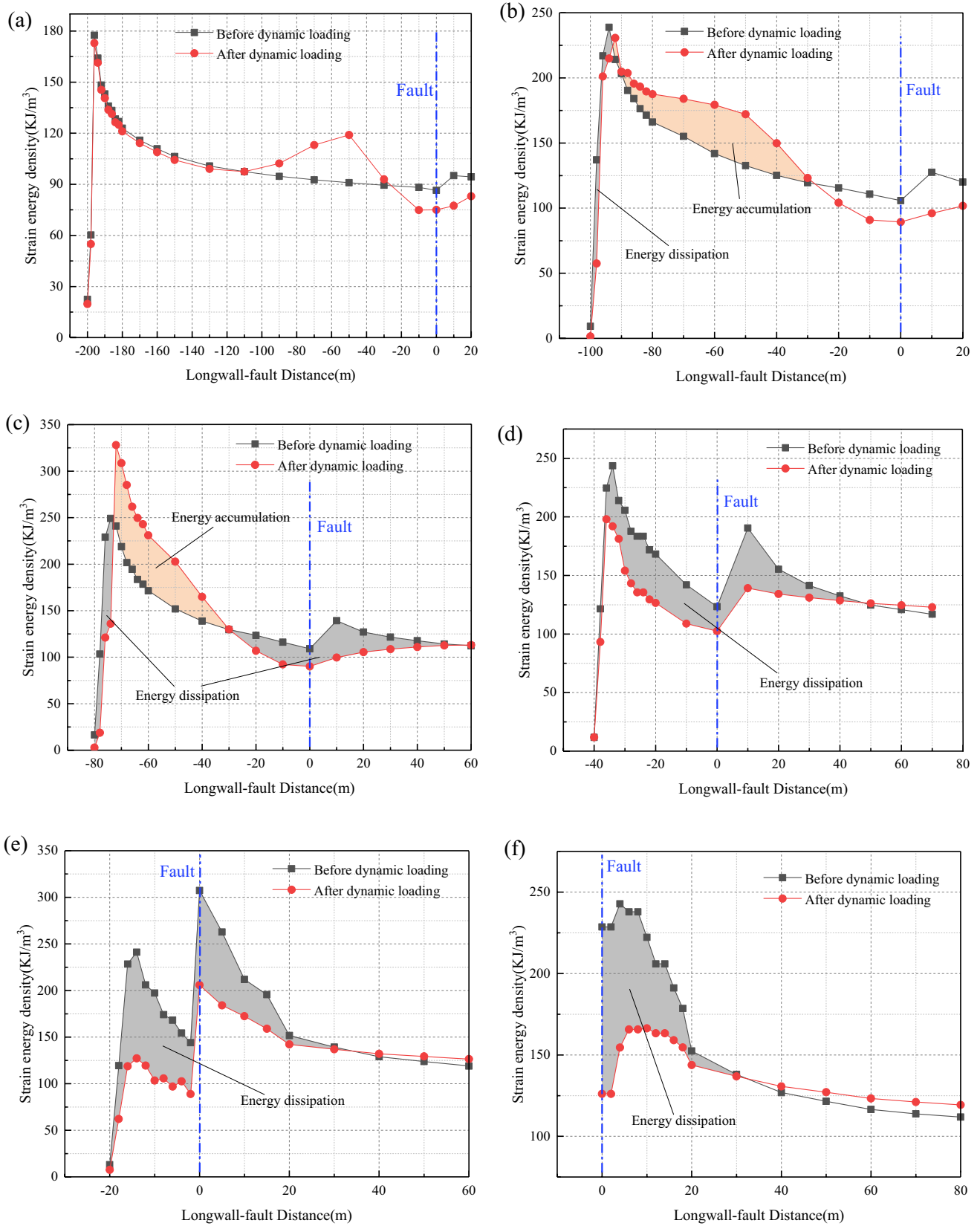


Fig. 14 Change law of SED in coal seam before and after the dynamic load. **a** Longwall–fault distance is 200 m. **b** Longwall–fault distance is 100 m. **c** Longwall–fault distance is 80 m. **d** Longwall–

fault distance is 40 m. **e** Longwall–fault distance is 20 m. **f** Longwall–fault distance is 0 m

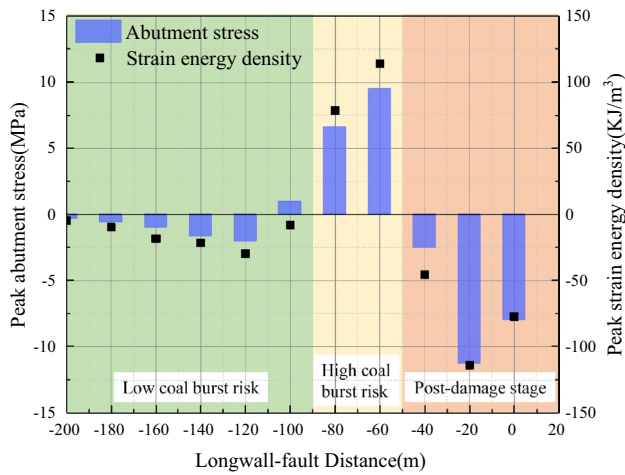


Fig. 15 Coal burst hazard classification

seam. When the longwall–fault distance is in the ranges of 200–80 m, 80–40 m, and 40–0 m, the coal seam is in the state of low coal burst risk, the state of high coal burst risk, and the post-damage stage, respectively.

4.5 Analysis of Coal Seam Destabilization Mechanism Under the Influence of Dynamic Fault-Slip Load

The internal energy field of the coal and rock mass evolves under dynamic loading. Figure 16 shows the SED evolution law in the coal seam after the dynamic loading effect of fault-slip.

Under the mining disturbance, the stress state around the fault changes, resulting in a sudden drop in shear stress and an increase in sliding displacement. The fault-slip release energy (E_s) is defined in Eq. (4) (Sainoki and Mitri 2014a):

$$E_s = 0.5\Delta\tau DS, \tag{4}$$

where $\Delta\tau$ is the stress drop defined as the average decrease between the shear stress on the fault before excavation and the shear stress after the excavation; D is the fault-slip displacement; S is the fault-slip area.

Fault-slip energy is transferred to the upper and lower rock masses, and the energy gradually decays. The received energy (E_r) at a certain point is (Liu et al. 2022):

$$E_r = E_s l^{-1} e^{-\eta l}, \tag{5}$$

where η is the energy attenuation coefficient, related to the magnitude of ground stress, stratigraphic fracture development, and other factors; l is the distance from the earthquake hypocenter to the longwall face.

As seen in Eq. (5), when the longwall face is far from the fault-slip seismic source, the energy decays in a negative exponential form. After the dynamic load is transferred to the coal seam near the longwall face, the residual energy is smaller, and the influence on the coal seam disturbance is reduced. In addition, the degree of fragmentation of the roof rock above the coal seam also affects the energy transfer process. As the roof is broken, the energy attenuation increases and the influence of fault activation shock on the coal seam decreases.

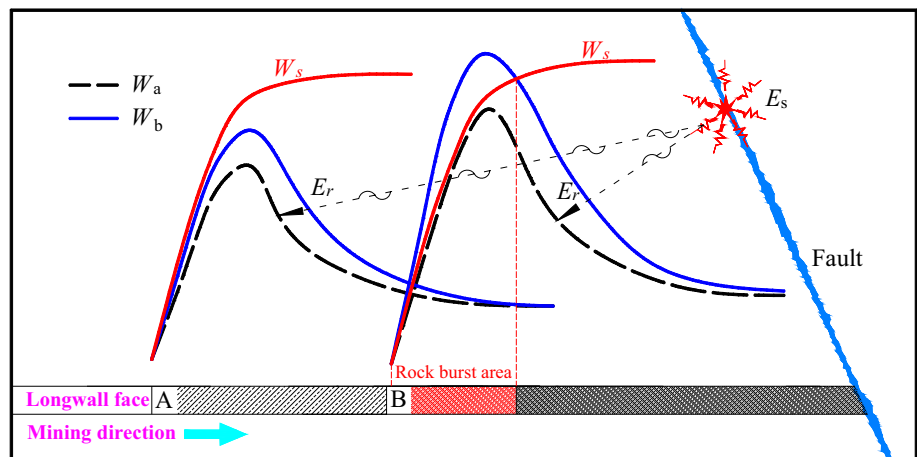
The strain energy stored in the coal seam is the primary source of coal bursts. The magnitude of the SED stored inside the coal seam before the effect of dynamic load disturbance is:

$$W_a = \left[\sigma_1'^2 + \sigma_2'^2 + \sigma_3'^2 - 2\nu'(\sigma_1'\sigma_2' + \sigma_2'\sigma_3' + \sigma_3'\sigma_1') \right] / 2E_0', \tag{6}$$

where $\sigma_1', \sigma_2', \sigma_3'$ are the maximum, intermediate and minimum principal stresses; ν' and E_0' are the Poisson's ratio and the elastic modulus of coal seam, respectively.

The strain energy has been stored inside the coal seam before being disturbed by the dynamic load. However, under the influence of dynamic load, the energy inside the coal

Fig. 16 Conceptual models of coal seam instability induced by fault-slip



seam is superimposed, and the superimposed energy equation is:

$$W_b = W_a + E_r/V, \quad (7)$$

$$W_b = \left[\sigma''_1{}^2 + \sigma''_2{}^2 + \sigma''_3{}^2 - 2\nu''(\sigma''_1\sigma''_2 + \sigma''_2\sigma''_3 + \sigma''_3\sigma''_1) \right] / 2E''_0, \quad (8)$$

where V is the unit volume; σ''_1 , σ''_2 , σ''_3 are the maximum, intermediate and minimum principal stresses after the action of dynamic load; ν'' and E''_0 are the Poisson's ratio and the elastic modulus of coal seam after the action of dynamic load, respectively.

The ultimate stored energy (energy storage limitation) (W_s) of the coal seam in the three-dimensional stress state can be used in Eq. (9) (Xie et al. 2005):

$$W_s = \frac{\sigma_c^3}{2E_0(\sigma_1 - \sigma_3)}, \quad (9)$$

where σ_c is the uniaxial compressive strength.

When the strain energy stored inside the coal seam exceeds its energy storage limitation, damage destabilization occurs inside the coal seam.

$$W_b \geq W_s. \quad (10)$$

The longwall face is far from the fault when its location is at point A, as shown in Fig. 16. At this time, the fault barrier does not affect the coal seam. The dynamic fault-slip load transfer to the longwall face is severely attenuated, so the strain energy stored inside the coal seam is smaller. At point A, W_b remains smaller than W_s , and the coal seam is stable. However, as the longwall face advances toward the fault, it reaches point B close to the fault. A significant amount of strain energy is stored inside the coal seam in front of point B due to the relative slip and barrier effect of the fault. After the dynamic fault-slip load, the energy superposition within the coal seam exceeds the energy storage limit, leading to destabilization damage of the coal seam with simultaneous release of strain energy. It can be seen that the high static load and strong dynamic load together lead to the occurrence of coal burst accidents.

5 Parametric Study and Results Analysis

The fault-slip releases the energy when the longwall face approaches the fault. As the distance between the longwall face and the fault decreases, the fault-slip location evolves from the high level of the fault far away from the coal seam to the location close to the coal seam and the floor, and the energy released gradually increases (Jiang et al. 2020; Wei et al. 2021). Therefore, investigation of coal seam stability

at different seismic energies and seismic positions has been carried out.

In this section, 11 models were conducted for the parametric study as shown in Table 3. Model 1 is the benchmark

model; its model parameters are shown in Sect. 3. Models 2–11 are established on the basis of Model 1. The energy magnitudes recorded for field microseismic monitoring data are 10^3 – 10^8 J, respectively, as shown in Fig. 2. When the seismic energy is less than 10^3 J, the dynamic load has no apparent effect on the coal seam disturbance, which is ignored in this study. Therefore, this study sets the source energy as 10^4 J, 10^5 J, 10^6 J, 10^7 J, and 10^8 J to investigate the influence of different source energy on the disturbance of the coal seam. The parameter settings of velocity vibration waves for different seismic energy are shown in Table 2. The location of seismic source were set at 70 m, 45 m, and 20 m from the roof of the coal seam, and 20 m from the floor of the coal seam, as shown in points 1, 2, 3, and 4 in Fig. 5.

According to Eq. (5), the fault-slip energy transfer is related not only to the magnitude of the source energy and propagation distance but also to the coefficient η . Generally, fissures in the roof and floor of a coal seam is developed and enriched with groundwater (Zuo et al. 2022). The coefficient η is influenced by the degree of fracture development, groundwater, ground stress, and other factors. Therefore, the study on the effect of dynamic fault-slip load on the stability of coal seam at different burial depths (400 m, 800 m, 1200 m, and 1600 m, as shown in Table 3) was carried out.

5.1 Impact of Seismic Energies

Figure 17a shows the change in PSED stored in the coal seam in front of the longwall face with the fault-slip

Table 3 Model parameters

Model	Buried depth (m)	Seismic energy (J)	Seismic location (m)
1	800	10^7	45
2	800	10^4	45
3	800	10^5	45
4	800	10^6	45
5	800	10^8	45
6	800	10^7	70
7	800	10^7	20
8	800	10^7	-20
9	400	10^7	45
10	1200	10^7	45
11	1600	10^7	45

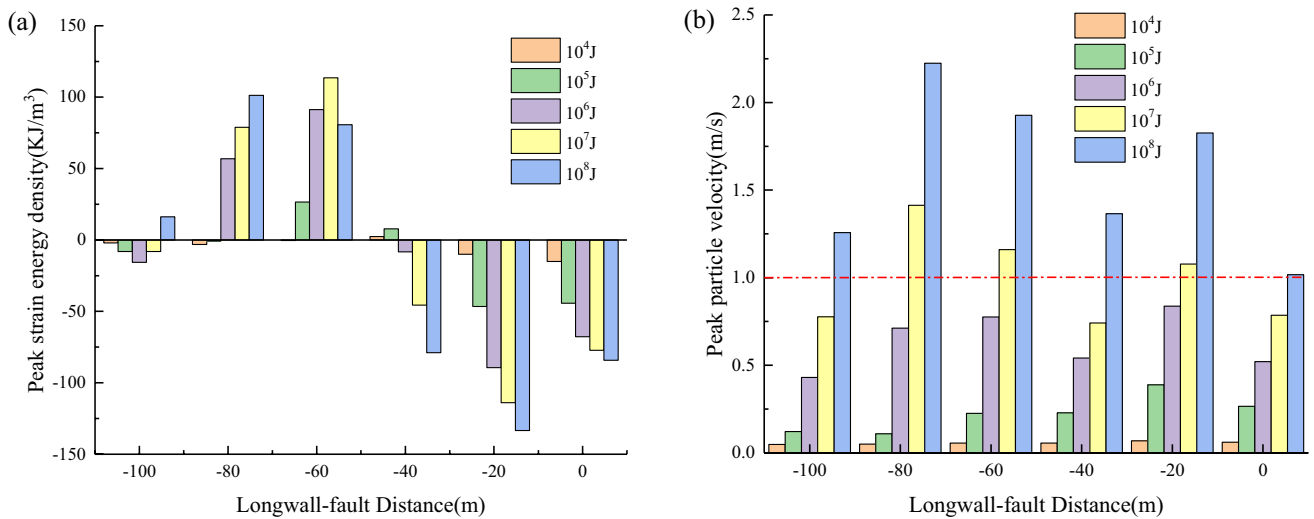


Fig. 17 Disturbance effect analysis of coal seam at different seismic energies. **a** Distribution of the PSED. **b** Distribution of the PVP

seismic energy. As the fault-slip seismic energy increases, the energy accumulated and released inside the coal seam increases. When the seismic energy is 10^4 J , the magnitude and location of the PSED do not change significantly after the dynamic fault-slip load. When the seismic energy is 10^5 J , a slight energy accumulation and release phenomenon occur inside the coal seam as the longwall–fault distance decreases. A seismic energy of 10^5 J can also induce a small coal burst event. When the seismic source energy exceeds 10^6 J , a significant accumulation and dissipation

of energy occur inside the coal seam after being subjected to the dynamic load. At the longwall–fault distance of 80 m, when the seismic energy is 10^6 J , 10^7 J , and 10^8 J , the location of PSED is 10 m, 12 m, and 14 m inside the rib, respectively, and the PSED is 305.90 kJ/m^3 , 328.04 kJ/m^3 and 350.35 kJ/m^3 , respectively, as shown in Fig. 18. With the increase in seismic energy, the depth of coal seam damage increases. When the seismic energy is 10^4 – 10^8 J and the longwall–fault distance is 20 m, the PSED release inside the coal seam after the fault-slip load is 9.99 kJ/m^3 ,

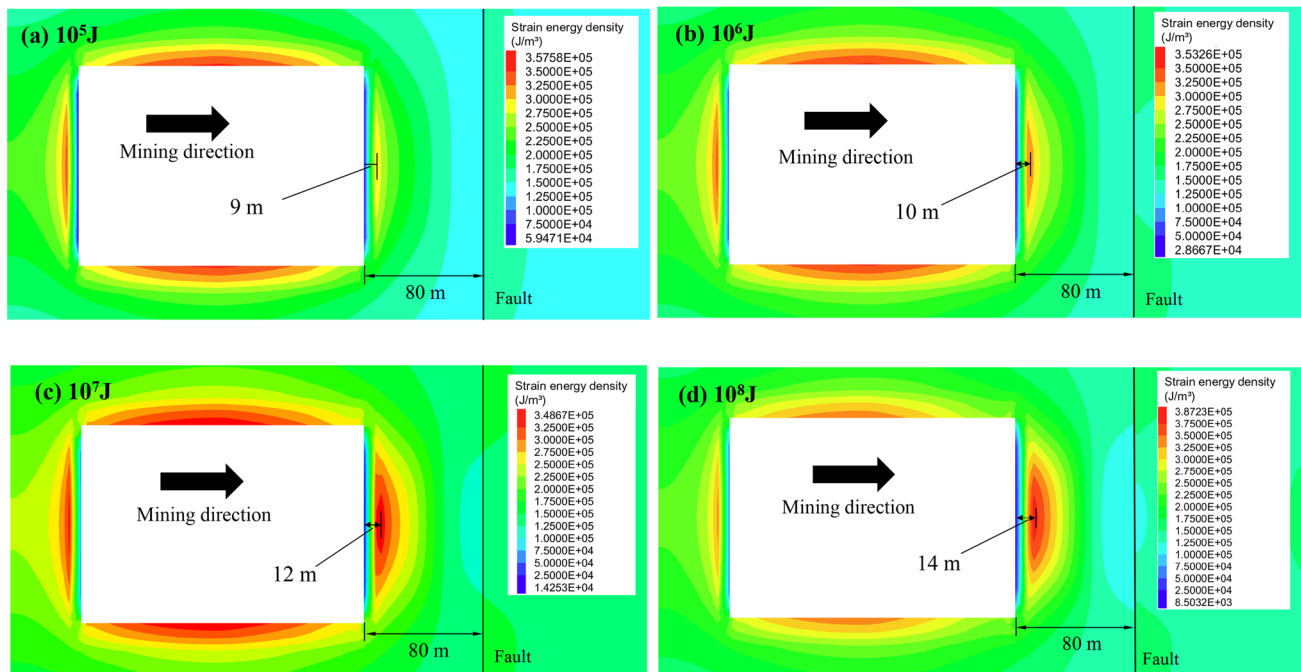


Fig. 18 The SED cloud diagram of coal seam at different seismic energies. **a** 10^5 J . **b** 10^6 J . **c** 10^7 J . **d** 10^8 J

46.57 kJ/m³, 89.46 kJ/m³, 113.92 kJ/m³, and 133.37 kJ/m³, respectively. With the growth of seismic energy, the coal burst potential increases significantly and the destructive force increases.

Figure 17b shows the PPV of the coal seam under different seismic energies. The PPV approaches or exceeds 1.0 m/s when the seismic energy exceeds 10⁶ J, which enhances the influence of the dynamic fault-slip load on the coal seam. When the seismic energy is 10⁴–10⁸ J and the longwall–fault distance is 20 m, the PPV magnitudes of the coal seam are 0.07 m/s, 0.39 m/s, 0.83 m/s, 1.08 m/s, and 1.83 m/s, respectively.

In general, when the fault-slip release energy exceeds 10⁶ J, the coal seam is susceptible to damage instability by the impact dynamic load. The damage depth of the coal seam increases continuously with increasing seismic energy.

However, with the increase in seismic energy, the dynamic load affects the coal seam within 80 m from the longwall face to the fault.

5.2 Impact of Seismic Source Locations

The variation pattern of PSED and PPV in the coal seam with the location of the dynamic fault-slip load, as shown in Fig. 19. The location of the seismic source as shown in Fig. 5. When the fault-slip position is located at point 1, there is no energy accumulation inside the coal seam as the longwall face advances toward the fault. The coal seam damage energy released is 52.23 kJ/m³ when the longwall–fault distance is 40 m. When the fault-slip position is located at point 2, 3, the PSED of the coal seam is accumulated

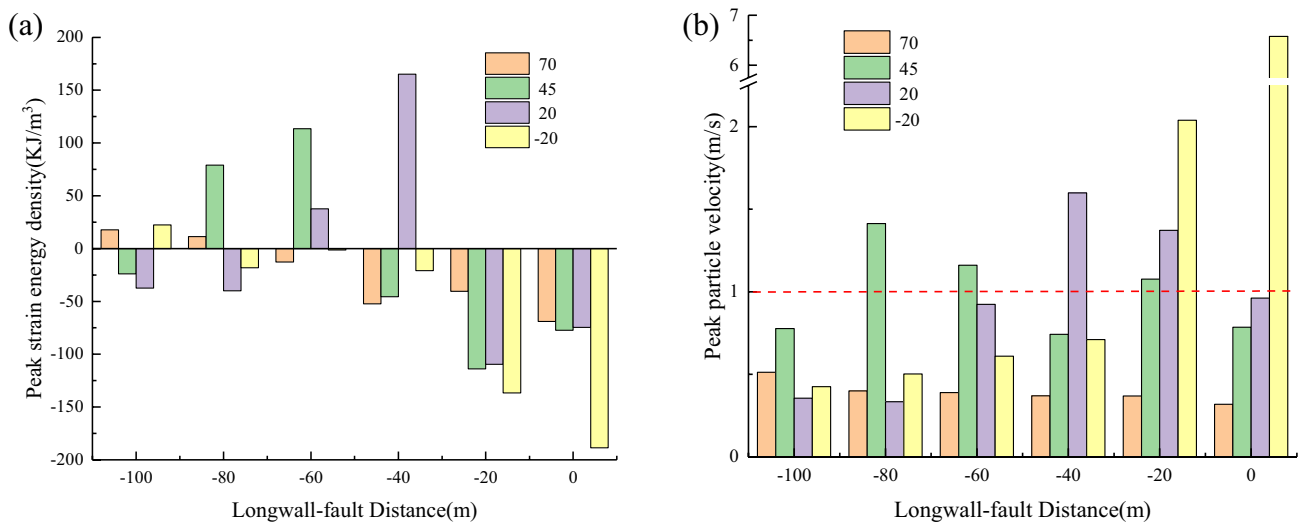


Fig. 19 Disturbance effect analysis of coal seam at different seismic source locations. a Distribution of the PSED. b Distribution of the PPV

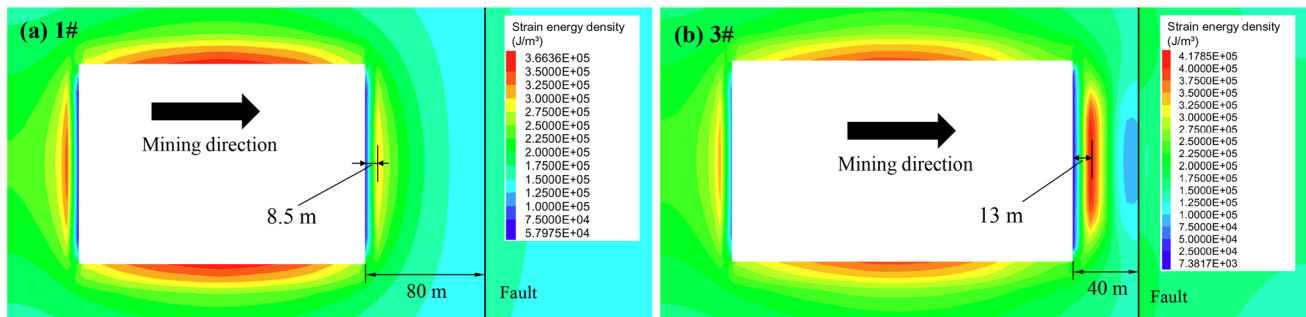


Fig. 20 The SED cloud diagram of coal seam at different seismic source locations. a Seismic location at point1. b Seismic location at point 3

at 78.94 kJ/m^3 and 165.11 kJ/m^3 after the longwall face advances to 80 m and 40 m from the fault. With the fault-slip continuously extending to the seam, the influence of dynamic load on the disturbance range of the coal seam decreases. When the fault-slip location is located at the floor, point 4 location, the dynamic load has a more negligible effect on the long-distance coal seam. However, when the longwall–fault distance is 20 m and 0 m, the coal seam damage energy released is 136.70 kJ/m^3 , 188.58 kJ/m^3 . A

significant accumulation of energy indicates an impact hazard within the coal seam. The energy accumulation occurs at 8.5 m, 12 m, and 13 m in front of the rib when the fault-slip position is points 1, 2, and 3, as shown in Figs. 18c, 20.

When the fault-slip position is 1, 2, 3, and 4 points, the PPV of the coal seam after the dynamic load is 0.51 m/s, 1.41 m/s, 1.60 m/s, and 6.58 m/s, and the PPV position is the longwall–fault distance 100 m, 80 m, 40 m, and 0 m, respectively. It is shown that the PPV and PSED of the coal seam

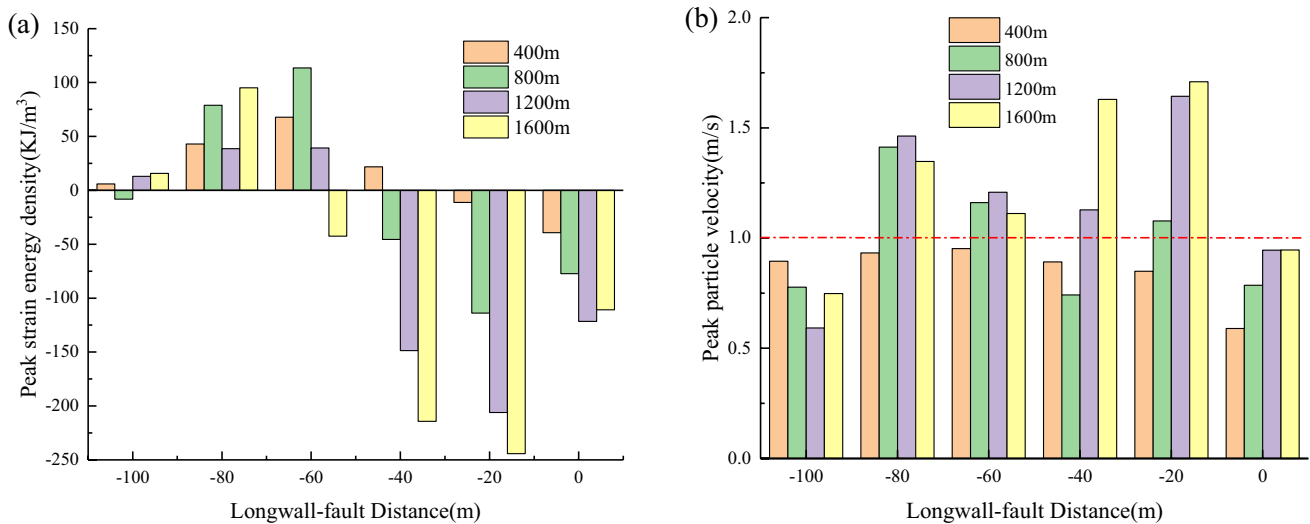


Fig. 21 Disturbance effect analysis of coal seam at different burial depths. a Distribution of the PSED. b Distribution of the PPV

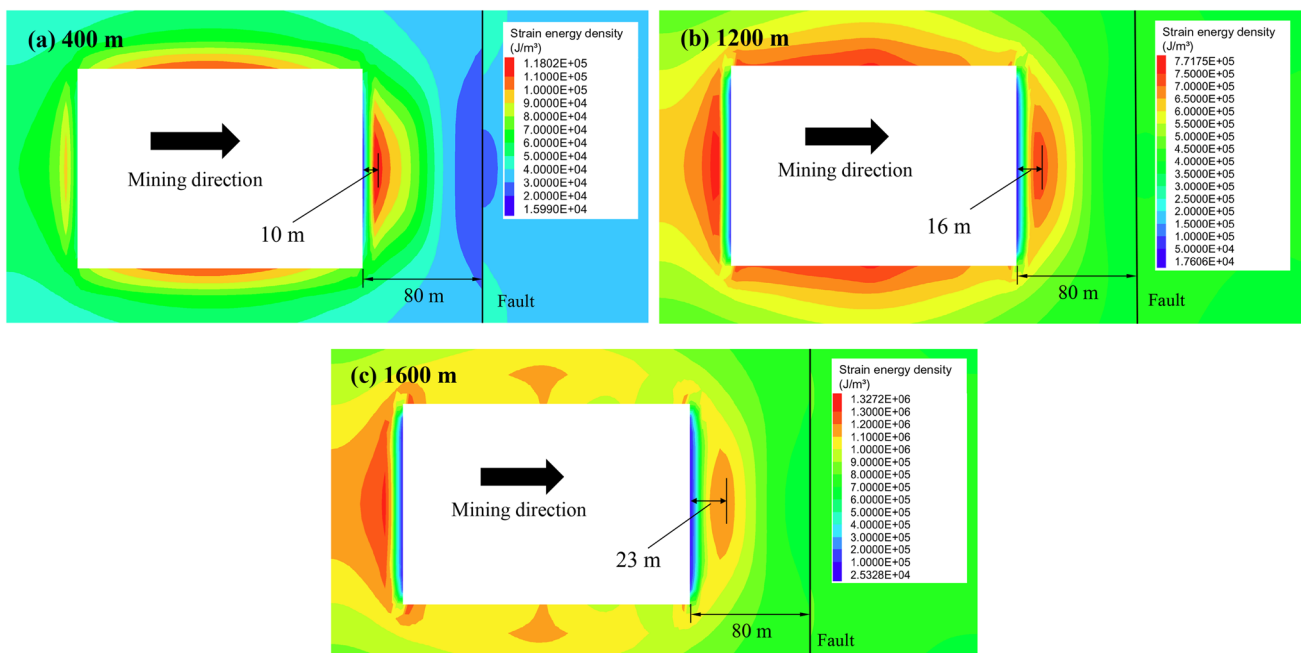


Fig. 22 The SED cloud diagram of coal seam at different burial depths. a Buried depth is 400 m. b Buried depth is 1200 m. c Buried depth is 1600 m

under the dynamic fault-slip load show a consistent pattern. Fault-slip continuously extends to the seam and the floor, the depth of coal seam damage increases, and the released energy of coal seam damage increases.

5.3 Impact of Burial Depths

As the cover depth increases, the PSED stored inside the coal seam increases. Figure 21 shows the trends of PSED and PPV in the coal seam with burial depth. The burial depths are 400 m, 800 m, 1200 m, and 1600 m, respectively. When the longwall–fault distance is 80 m, the magnitudes of energy accumulated inside the coal seam after the dynamic load at different burial depths (from 400 to 1600 m) are 42.94 kJ/m³, 78.94 kJ/m³, 38.60 kJ/m³, and 95.14 kJ/m³, respectively. The location of the PSED under different burial depth conditions after the dynamic load is shown in Figs. 18c and 22. The damage depth of the coal seam is positively correlated with the burial depth, and the PSED locations are at 10 m, 12 m, 16 m, and 23 m from the rib. When the longwall–fault distance is 20 m, the energy released during the coal seam damage is 11.20 kJ/m³, 113.92 kJ/m³, 206.14 kJ/m³, 244.25 kJ/m³, respectively. Therefore, as the burial depth increases, the ground stress level increases, and the degree of fracture development of the rock layer decreases, so that the extent of energy transfer attenuation decreases.

The PPV of the coal seam is less than 1.0 m/s after dynamic loading at a burial depth of 400 m, as shown in Fig. 21b. The seismic energy is severely attenuated at a burial depth of 400 m, leading to a more negligible effect of the dynamic load on the coal seam. When the burial depth exceeds 800 m, the PPV increases with increasing burial depth, which means that the ground stress size determines the energy transfer efficiency.

6 Discussion

During recovery of the 25,110 longwall face, the F16 fault-slip was induced to release energy, which led to a coal burst accident. The four parameters, including vibration velocity, displacement of rib, abutment stress, and SED, can be used to determine the stability of a coal seam after the effect of a dynamic fault-slip load. As the longwall–fault distance decreases, the internal abutment stress and SED of the coal seam increase due to the influence of the fault blocking effect (Chen et al. 2012). After the dynamic fault-slip load, the vibration velocity in the coal seam gradually increases and induces horizontal displacement (toward the longwall face) of the rib. The superposition of the fault-slip energy and the strain energy stored inside the coal seam exceeds the energy storage limitation, which reduces the stability

of the coal seam. Cai and Dou et al. (2021) proposed that fault-induced coal bursts are triggered by the superposition of high static stress in the fault pillar and dynamic stress from fault reactivation. Under the conditions of high static load, strong dynamic load, and low critical stress, coal burst accidents frequently occur. The numerical simulation results in this study verify the fault-slip-induced coal burst mechanism.

As the longwall face approaches the fault, the coal burst potential significantly increases (Jiang et al. 2020). Wei et al. (2020, 2021) found that PSED showed a drastic increase across longwall–fault distances of 45 m to 25 m, and PSED showed the most significant drop as longwall–fault distance changed from 25 to 0 m. In this study, the strain energy accumulates in the coal seam at the longwall–fault distance between 80 and 40 m, and the strain energy releases at the longwall–fault distance between 40 and 0 m, as shown in Fig. 14. The influence of dynamic fault-slip load possibly caused the energy superposition to occur inside the coal seam, increasing the damaged area. As Lu et al. (2019) noted, the "8.11" severe coal burst accident occurred when the longwall–fault distance was less than 100 m. Therefore, in this study, the longwall–fault distance is 80–40 m, defined as a high-risk coal burst area, and the longwall–fault distance is 40–0 m, defined as the coal seam damaged area.

The SED index combined with PPV and abutment pressure can better reflect the stability of the coal seam. However, it should be noted that SED is not really a fully representative indicator for seismic hazards because SED can be very high with no bursting likelihood at all. Based on the method of overall energy balance of the model, the size of the radiated seismic energy released when the coal seam is destroyed can be analyzed to better evaluate the coal burst potential (Poeck et al. 2016; Garvey and Ozbay 2013; Khademian and Ozbay 2018). The loading system stiffness determines how much energy if any can be released from coal failure (Salamon 1970; Gu and Ozbay 2014, 2015). In the future, by analyzing the energy available from the loading system and energy consumed by the failure, the energy released by impact failure can be calculated to analyze the coal burst potential.

In this study, there is no attention to the treatment of the mined-out area after the excavation of the longwall face. In FLAC3D, there are generally three types of materials used to simulate the mined-out area: Double-Yield constitutive model material (Yavuz 2004; Shabanimashcool et al. 2012; Zhang et al. 2015), non-linear elastic material (Si et al. 2015), and soft elastic material (Wang et al. 2013; Basarir et al. 2015; Wei et al. 2020). In the future, the excavation can be simulated with replacing the original materials in the mined-out area by a weak material representing the goaf material. With more accurate results on the deformation and movement of overlying strata and the stress redistribution around

the longwall excavations, the Mohr–Coulomb strain-softening (MCSS) model outperforms other constitutive models in simulating the laminated rock layers in longwall mining (Zareifard 2020; Wei et al. 2020). One future direction of research is the improvement of the intrinsic structure model.

Fault-induced coal bursts under mining, which means that effective coal bursts control measures must be applied. Generally speaking, there are three methods to prevent and control coal burst accidents as follows: (1) microseismic monitoring, seismic tomography, and other techniques to assess the risk of coal bursts (Zhang et al. 2021; Wang et al. 2017a; Gong et al. 2019); (2) drilling large diameter boreholes, directional hydraulic fracturing boreholes, and floor pressure relief boreholes in the coal burst area to advance energy release (Hua et al. 2001; Li et al. 2014; Zhao et al. 2018; Manouchehrian et al. 2021); (3) select rock support bracket with good energy absorption capacity (Li 2010; Wang et al. 2022; Jia et al. 2021). In follow-up research, coal burst prevention and control research under high static load and strong dynamic load conditions will be carried out. First, drilling large diameter boreholes in the high-stress and high-energy areas of the coal seam will be carried out to reduce the static load and release energy. Second, precracked blasting of the roof will be carried out to improve the degree of roof fragmentation and reduce the dynamic load transfer coefficient. Finally, a rock bolt will be implemented to improve the energy storage limitation of the coal and rock mass.

7 Conclusion

Through numerical simulation, this study demonstrated the coal burst mechanism induced by fault-slip energy release. Combined with an engineering case, the effect of the dynamic load from fault activation on coal seam disturbance when the longwall face advances toward the fault is studied, to determine the stability of the coal seam after superposition of dynamic and static loads. The main conclusions drawn from the study are summarized below.

(1) Parameters of the coal seam, including vibration velocity, rib displacement, abutment stress, and SED, can be used to effectively assess the stability of the coal seam before and after the influence of dynamic fault-slip load. The sudden increase in the vibration velocity, displacement, abutment stress, and SED of the coal seam is the precursor to a coal burst.

(2) The PAS and the PSED show similar trends. Blocked by the fault, the SED stored inside the coal seam increases as the longwall–fault distance decreases, and the coal seam is in a high static load state. Under the action of dynamic fault-slip loading, the impact energy is transferred to the inside of the coal seam. A high static load and a strong dynamic

load are superimposed on the coal seam, resulting in the accumulation and rapid release of SED inside the coal seam and the occurrence of impact accidents.

(3) According to the change in longwall–fault distance, the risk of coal burst is divided into three levels. When the longwall–fault distance is 200–80 m, 80–40 m, and 40–0 m, the coal seam is in the state of low coal burst risk, the state of high coal burst risk, and the post-damage stage, respectively. Therefore, when the longwall–fault distance is less than 80 m, it is necessary to strengthen the protection to prevent coal burst accidents.

(4) In the parametric study, the effect of seismic load on the disturbance of coal seam is analyzed for different seismic energies, seismic locations, and burial depths. For the effects of seismic energy and burial depth, the results show that the coal seam is subjected to increased dynamic loading with the increase in seismic energy, and, with the increase in burial depth, the static loading of the coal seam increases after mining. The combination of high static load and strong dynamic load leads to an increase in energy released during coal bursts and an increase in rib damage depth. The results for the effect of seismic location show that with the fault-slip continuously extending to the seam and the floor, the effect range of dynamic load on the coal seam decreases, but the damage depth of the rib increases.

Acknowledgements This research was supported by the Natural Science Foundation of Shandong Province (ZR2016EEM36).

Data availability The data that support the findings of this study are available on request from the corresponding author upon reasonable request.

Declarations

Conflict of Interest The authors declare that they have no conflict of interest.

References

- Basarir H, Oge IF, Aydin O (2015) Prediction of the stresses around main and tail gates during top coal caving by 3D numerical analysis. *Int J Rock Mech Min Sci* 76:88–97
- Brace WF, Byerlee JD (1966) Stick-slip as a mechanism for earthquake. *Science* 153(3739):990–992
- Brinkmann JR (1987) Separating shock wave and gas expansion breakage mechanism. In: 2nd International Symposium on Rock Fragmentation by Blasting, pp 6–15
- Cai W, Dou LM, Cao AY, Gong SY, Li ZL (2014) Application of seismic velocity tomography in underground coal mines: a case study of Yima mining area, Henan. *China J Appl Geophys* 109:140–149
- Cai W, Dou LM, Si GY, Hu YW (2021) Fault-induced coal burst mechanism under mining-induced static and dynamic stresses. *Engineering* 7:687–700
- Chen XH, Li WQ, Yan XY (2012) Analysis on rock burst danger when fully-mechanized caving coal face passed fault with deep mining. *Saf Sci* 50(4):645–648

- Cheng GW, Li LC, Zhu WC, Yang TH, Tang CA, Zheng Y, Wang Y (2019) Microseismic investigation of mining-induced brittle fault activation in a Chinese coal mine. *Int J Rock Mech Min Sci* 123:104096
- Dai LP, Pan YS, Li ZH, Wang AW, Xiao YH, Liu FY, Shi TW, Zheng WH (2021) Quantitative mechanism of roadway rockbursts in deep extra-thick coal seams: theory and case histories. *Tunnel Undergr Space Technol* 111:103–116
- Dou LM, Mu ZL, Li ZL, Cao AY, Gong SY (2014) Research progress of monitoring, forecasting, and prevention of rockburst in underground coal mining in China. *Int J Coal Sci Technol* 1(3):278–288
- Gao FQ, Kang HP, Li JZ (2021) Numerical simulation of fault-slip rockbursts using the distinct element method. *Tunn Undergr Space Technol* 110:103805
- Garvey R, Ozbay U (2013) Assessing coal bumps from excess energy in finite difference models. In: *Proceedings of the 11th International Conference on Ground Control in Mining*
- Gong SY, Li J, Ju F, Dou LM, He J, Tian XY (2019) Passive seismic tomography for rockburst risk identification based on adaptive grid method. *Tunn Undergr Space Technol* 86:198–208
- Gu R, Ozbay U (2014) Distinct element analysis of unstable shear failure of rock discontinuities in underground mining conditions. *Int J Rock Mech Min Sci* 68:44–54
- Gu R, Ozbay U (2015) Numerical investigation of unstable rock failure in underground mining condition. *Comput Geotechnol* 63:171–182
- He MC, Ren FQ, Liu DQ (2018) Rockburst mechanism research and its control. *Int J Min Sci Technol* 28(5):829–837
- Hua AZ, You MQ (2001) Rock failure due to energy release during unloading and application to underground rock burst control. *Tunn Undergr Space Technol* 16(3):241–246
- Itasca (2009) *FLAC3D-fast Lagrangian analysis of continua*. Itasca Consulting Group Inc, Washington
- Jia HS, Wang YW, Liu SW, Wang L, Zhi GH, Peng B, Li YE (2021) Experimental study of stirring and resin-blocking devices for improving the performance of resin-anchored cable bolts. *Rock Mech Rock Eng* 54(8):3995–4008
- Jiang YD, Zhao YX, Wang HW, Zhu J (2017a) A review of mechanism and prevention technologies of coal bumps in China. *J Rock Mech Geotech Eng* 9(4):180–194
- Jiang LS, Wang P, Zhang PP, Zheng PQ, Xu B (2017b) Numerical analysis of the effects induced by normal faults and dip angles on rock bursts. *CR Mech* 345:690–705
- Jiang LS, Kong P, Zhang PP, Shu JM, Wang QB, Chen LJ, Wu QL (2020) Dynamic analysis of the rock burst potential of a longwall panel intersecting with a fault. *Rock Mech Rock Eng* 53:1737–1754
- Jiao ZH, Wang L, Zhang M, Wang J (2021) Numerical simulation of mining-induced stress evolution and fault-slip behavior in deep mining. *Adv Mater Sci Eng* 2021:8276408
- Khademian Z, Ozbay U (2018) Computational framework for simulating rock burst in shear and compression. *Int J Rock Mech Min Sci* 110:279–290
- Kong P, Jiang LS, Shu JM, Sainoki A, Wang QB (2019) Effect of fracture heterogeneity on rock mass stability in a highly heterogeneous underground roadway. *Rock Mech Rock Eng* 52(11):4547–4564
- Li CC (2010) A new energy-absorbing bolt for rock support in high stress rock masses. *Int J Rock Mech Min* 47(3):396–404
- Li ZL, Dou LM, Cai W, Wang GF, He J, Gong SY, Ding YL (2014) Investigation and analysis of the rock burst mechanism induced within fault-pillars. *Int J Rock Mech Min Sci* 70:192–200
- Li ZL, Dou LM, Cai W, Wang GF, Ding YL, Kong Y (2016) Mechanical analysis of static stress within fault-pillars based on a voussoir beam structure. *Rock Mech Rock Eng* 49:1097–1105
- Li CC, Mikula P, Simser B, Hebblewhite B, Joughin W, Feng XW, Xu NW (2019) Discussions on rockburst and dynamic ground support in deep mines. *J Rock Mech Geotech Eng* 11(5):1110–1118
- Li ZL, Wang CH, Shan RL, Yuan HH, Zhao Y, Wei YH (2021) Study on the influence of the fault dip angle on the stress evolution and slip risk of normal faults in mining. *Bull Eng Geol Environ* 80(5):3537–3551
- Liu H, Yu B, Liu JR, Wang TX (2019) Investigation of impact rock burst induced by energy released from hard rock fractures. *Arab J Geosci* 12:381
- Liu YQ, Cao AY, Wang SW, Yang Y, Guo WH, Xue CC, Li XW (2022) Attenuation characteristics analysis of seismic energy and its application to risk assessment in underground coal mines. *Geomatics Nat Hazards Risk* 13(1):1014–1042
- Lizurek G, Rudzinski L, Plesiewicz B (2015) Mining induced seismic event on an inactive fault. *Acta Geophys* 63(1):176–200
- Lu CP, Liu B, Liu B, Liu Y, Wang HY, Heng Z (2019) Anatomy of mining-induced fault-slip and a triggered rockburst. *Bull Eng Geol Environ* 78(7):5147–5160
- Manouchehrian A, Kulatilake PHSW, Wu R (2021) Strainburst control in deep tunnels using a slotted excavation method. *Int J Geomech* 22(4):04022008
- Miao SJ, Cai MF, Guo QF, Huang ZJ (2016) Rock burst prediction based on in-situ stress and energy accumulation theory. *Int J Rock Mech Min Sci* 83:86–94
- Mutke G, Dubiński J, Lurka A (2015) New criteria to assess seismic and rock burst hazard in coal mines. *Arch Min Sci* 60:743–760
- Ortlepp WD (2000) Observation of mining-induced faults in an intact rock mass at depth. *Int J Rock Mech Min Sci* 37(1):423–436
- Poecck E, Khademian Z, Garvey R, Ozbay U (2016) Modeling unstable rock failures in underground excavations. In: *Proceedings of 2016 ISRM International Symposium: Rock Mechanics and Rock Engineering: From the Past to the Future*, pp 505–509
- Sainoki A, Mitri HS (2014a) Dynamic behaviour of mining-induced fault-slip. *Int J Rock Mech Min Sci* 66(1):19–29
- Sainoki A, Mitri HS (2014b) Dynamic modelling of fault-slip with barton's shear strength model. *Int J Rock Mech Min Sci* 67(67):155–163
- Sainoki A, Mitri HS (2014c) Simulating intense shock pulses due to asperities during fault-slip. *J Appl Geophys* 103:71–81
- Sainoki A, Mitri HS (2015) Effect of slip-weakening distance on selected seismic source parameters of mining-induced fault-slip. *Int J Rock Mech Min Sci* 73:115–122
- Sainoki A, Mitri HS (2018) Quantitative analysis with plastic strain indicators to estimate damage induced by fault-slip. *J Rock Mech Geotech Eng* 10(1):1–10
- Salamon MDG (1970) Stability, instability and design of pillar workings. *Int J Rock Mech Min Sci* 7(6):613–631
- Shabanimashcool M, Li CC (2012) Numerical modelling of longwall mining and stability analysis of the gates in a coal mine. *Int J Rock Mech Min Sci* 51:24–34
- Si GY, Shi JQ, Durucan S, Korre A, Lazar J, Jamnikar S, Zavšek S (2015) Monitoring and modelling of gas dynamics in multi-level longwall top coal caving of ultra-thick coal seams. Part II: numerical modelling. *Int J Coal Geol* 144:58–70
- Wang X, Cai M (2017) Numerical modeling of seismic wave propagation and ground motion in underground mines. *Tunn Undergr Space Technol* 68:211–230
- Wang HW, Jiang YD, Zhao YX, Zhu J, Liu S (2013) Numerical investigation of the dynamic mechanical state of a coal pillar during longwall mining panel extraction. *Rock Mech Rock Eng* 46(5):1211–1221
- Wang GF, Gong SY, Li ZL, Dou LM, Cai W, Mao Y (2015) Evolution of stress concentration and energy release before rock bursts: two case studies from Xingan coal mine, Hegang. *China Rock Mech Rock Eng* 49(8):3393–3401

- Wang CB, Cao AY, Zhu GA, Jing GC, Li J, Chen T (2017) Mechanism of rock burst induced by fault-slip in an island coal panel and hazard assessment using seismic tomography: a case study from Xuzhuang colliery, Xuzhou. *China Geosci J* 21(3):469–481
- Wang HW, Shi RM, Lu CS, Jiang YD, Deng DX, Zhang DQ (2019) Investigation of sudden faults instability induced by coal mining. *Saf Sci* 115:256–264
- Wang HW, Xue S, Shi RM, Jiang YS, Gong WL, Mao LT (2020) Investigation of fault displacement evolution during extraction in longwall panel in an underground coal mine. *Rock Mech Rock Eng* 53(10):1809–1826
- Wang HW, Shi RM, Deng DX, Cui F, Jiang YD (2021a) A calculation methodology of fault relative displacement used to study the mechanical characteristic of fault slip. *J Geophys Eng* 18:920–942
- Wang HW, Shi RM, Song JQ, Tian Z, Deng DX, Jiang YD (2021b) Mechanical model for the calculation of stress distribution on fault surface during the underground coal seam mining. *Int J Rock Mech Min Sci* 144:104765
- Wang W, Pan YS, Xiao YH (2022) Synergistic mechanism and technology of cable bolt resin anchoring for roadway roofs with weak interlayers. *Rock Mech Rock Eng* 55:3451–3472
- Wei CC, Zhang CG, Canbulat I (2020) Numerical analysis of fault-slip behaviour in longwall mining using linear slip weakening law. *Tunn Undergr Space Technol* 104:103541
- Wei CC, Zhang CG, Canbulat I, Huang WP (2021) Numerical investigation into impacts of major fault on coal burst in longwall mining: a case study. *Int J Rock Mech Min Sci* 147:104907
- Xiao P, Li D, Zhao G, Liu H (2021) New criterion for the spalling failure of deep rock engineering based on energy release. *Int J Rock Mech Min Sci* 148:1–12
- Xie HP, Ju Y, Li LY (2005) Criteria for strength and structural failure of rocks based on energy dissipation and energy release principles. *Chin J Rock Mech Eng* 24(17):3003–3010 (in Chinese)
- Xing H, Han Z (2020) Caving-induced fault reactivation behaviour and its effects on mining safety with a multiple seam context. *Acta Geotech* 15(12):3461–3481
- Yavuz H (2004) An estimation method for cover pressure re-establishment distance and pressure distribution in the goaf of longwall coal mines. *Int J Rock Mech Min Sci* 41(2):193–205
- Zareifard MR (2020) Ground reaction curve for deep circular tunnels in strain softening Mohr-Coulomb rock masses considering the damaged zone. *Int J Geomech* 20(10):04020190
- Zhang ZZ, Bai JB, Chen Y, Yan S (2015) An innovative approach for gob-side entry retaining in highly gassy fully-mechanized longwall top-coal caving. *Int J Rock Mech Min Sci* 80:1–11
- Zhang C, Jin G, Liu C, Li S, Xue J, Cheng R, Wang XL, Zeng XZ (2021) Prediction of rockbursts in a typical island working face of a coal mine through microseismic monitoring technology. *Tunn Undergr Space Technol* 113:103972
- Zhao TB, Guo WY, Tan YL, Yin YC, Cai LS, Pan JF (2018) Case studies of rock bursts under complicated geological conditions during multi-seam mining at a depth of 800 m. *Rock Mech Rock Eng* 51:1539–1564
- Zuo JP, Wu GS, Du J, Lei B, Li YB (2022) Rock strata failure behavior of deep ordovician limestone aquifer and multi-level control technology of water inrush based on microseismic monitoring and numerical methods. *Rock Mech Rock Eng* 55:4591–4614

Publisher's Note Springer Nature remains neutral with regard to jurisdictional claims in published maps and institutional affiliations.

Springer Nature or its licensor (e.g. a society or other partner) holds exclusive rights to this article under a publishing agreement with the author(s) or other rightsholder(s); author self-archiving of the accepted manuscript version of this article is solely governed by the terms of such publishing agreement and applicable law.